Materials Horizons

ROYAL SOCIETY OF CHEMISTRY

REVIEW

View Article Online
View Journal | View Issue

Cite this: *Mater. Horiz.*, 2025, **12**, 2089

Layered double hydroxide modified bismuth vanadate as an efficient photoanode for enhancing photoelectrochemical water splitting

Md. Masum Billah [ab] and Go Kawamura*[a]

Photoelectrochemical (PEC) water splitting has attracted significant interest as a promising approach for producing clean and sustainable hydrogen fuel. An efficient photoanode is critical for enhancing PEC water splitting. Bismuth vanadate ($BiVO_4$) is a widely recognized photoanode for PEC applications due to its visible light absorption, suitable valence band position for water oxidation, and outstanding potential for modifications. Nevertheless, sluggish water oxidation rates, severe charge recombination, limited hole diffusion length, and inadequate electron transport properties restrict the PEC performance of $BiVO_4$. To surmount these constraints, incorporating layered double hydroxides (LDHs) onto $BiVO_4$ photoanodes has emerged as a promising approach for enhancing the performance. Herein, the latest advancements in employing LDHs to decorate $BiVO_4$ photoanodes for enhancing PEC water splitting have been thoroughly studied and outlined. Initially, the fundamental principles of PEC water splitting and the roles of LDHs are summarized. Secondly, it covers the development of different composite structures, including $BiVO_4$ combined with bimetallic and trimetallic LDHs, as well as other $BiVO_4$-based composites such as $BiVO_4$/metal oxide, metal sulfide, and various charge transport layers integrated with LDHs. Additionally, LDH composites incorporating materials like graphene, carbon dots, quantum dots, single-atom catalysts, and techniques for surface engineering and LDH exfoliation with $BiVO_4$ are discussed. The research analyzes the design principles of these composites, with a specific focus on how LDHs enhance the performance of $BiVO_4$ by increasing the efficiency and stability through synergistic effects. Finally, challenges and perspectives in future research toward developing efficient and stable $BiVO_4$/LDHs photoelectrodes for PEC water splitting are described.

Received 29th October 2024,
Accepted 18th December 2024

DOI: 10.1039/d4mh01533a

rsc.li/materials-horizons

[a] *Department of Electrical and Electronic Information Engineering, Toyohashi University of Technology, 1-1 Hibarigaoka, Tempaku-cho, Toyohashi, 441-8580, Aichi, Japan. E-mail: kawamura.go.km@tut.jp*

[b] *Department of Chemistry, Comilla University, Cumilla-3506, Bangladesh*

Md. Masum Billah

Md. Masum Billah is pursuing his PhD in Electrical and Electronic Information Engineering at Toyohashi University of Technology under the supervision of Professor Dr Go Kawamura. He obtained his B.Sc. and M.S. degrees in Chemistry from the University of Chittagong in 2014 and 2016, respectively. Since 2020, he has been an Assistant Professor in the Department of Chemistry at Comilla University, Bangladesh. His current research interest is focused on the development of new photoelectrodes based on bismuth vanadate and solar hydrogen production technology.

Go Kawamura

Go Kawamura is an associate professor in Toyohashi University of Technology. He obtained his PhD degree from Nagoya Institute of Technology in 2009, then he started working at Toyohashi University of Technology. His current research interests are focused on the development of photocatalysts and photoelectrodes for solar water splitting and tackling environmental and energy issues.

Wider impact

This review presents recent advancements in layered double hydroxide (LDH) modified $BiVO_4$ photoanodes for efficient PEC water splitting. First, we outline the fundamental principles of photoelectrochemical (PEC) water splitting and the roles of LDHs in improving efficiency and stability. The development of various composite structures, including $BiVO_4$ with bimetallic and trimetallic LDHs, and $BiVO_4$-based composites with metal oxides, metal sulfides, and charge transport layers is summarized. Additionally, we discuss LDH composites incorporating graphene, carbon dots, quantum dots, and single-atom catalysts, along with techniques for surface engineering and LDH exfoliation with $BiVO_4$. This research contributes to scalable green hydrogen generation, decarbonizing industries, ensuring energy security, and mitigating climate change, aligning with global sustainability goals (SDGs 7 and 13), advancing the transition to sustainable society. Despite progress in coupling LDHs with $BiVO_4$ photoanodes for PEC water splitting, challenges like interfacial recombination, stability, and conductivity remain. Future research will focus on interface engineering, optimized LDH loading, and exploring intercalated anions. Advanced tandem systems using LDH modified $BiVO_4$ photoanodes will offer promising, cost-effective pathways for improving PEC performance, shaping the development of next generation techniques and driving innovations in energy conversion, storage, and environment conservation.

1. Introduction

Due to the rapid increase in world population and industrialization, energy demand is expected to increase from 20 TW to 40 TW by 2050.[1–3] Currently, about 85% of our energy comes from nonrenewable energy sources, such as coal, oil, and natural gas.[4,5] Nevertheless, these sources are unsustainable and release carbon dioxide (CO_2), carbon monoxide (CO), nitrogen oxides (NO_x), sulfur oxides (SO_x), and other pollutants, which have serious consequences for the environment and human health, ultimately resulting in catastrophic climate change and global warming.[6–9]

To address these challenges, research into sustainable and renewable energy generation technologies is crucial. Solar energy, among all sustainable sources, is the most plentiful, inexhaustible, and widely distributed renewable energy source on Earth.[10] Every year, about 100 000 TW of solar energy comes from the sun, of which approximately 36 000 TW reaches the earth.[11] It is suggested that the amount of solar radiation that reaches the Earth's surface per h is sufficient to meet the planet's energy needs for a whole year.[12,13] Nonetheless, the effectiveness of solar energy conversion and storage encounters obstacles due to its erratic nature, as well as seasonal and regional variations.[14–17] Therefore, it is essential to develop technologies that can effectively capture and utilize solar energy to produce clean and sustainable fuel. Among the various solar energy conversion strategies, solar-driven water splitting is an effective approach for converting solar energy into hydrogen (H_2).[18] H_2 produced by the overall solar water splitting process is referred to as green H_2 because it does not emit any carbon dioxide.[19,20] As a fuel with high density, it possesses the advantageous characteristics of being both storable and transportable.[21] Moreover, it finds extensive application in various industries as chemical feedstock, particularly in the production of ammonia, the reduction of carbon dioxide into liquid synthetic fuel and in fuel cells to generate electricity.[22–24] As a green and renewable energy source, solar hydrogen can also meet future energy needs and address environmental concerns.[25]

Currently, the three most relevant solar hydrogen production processes are (i) photovoltaic assisted electrolysis (PV-E), (ii) photocatalysis (PC), and (iii) photoelectrochemical (PEC) water splitting. Non-integrated PV-E technology, with its high solar-to-hydrogen (STH) efficiency and mature technological base, is the most practical configuration and has been optimized over decades.[26] However, hydrogen production using this method is too expensive due to the high complexity of the cell design.[27,28] In contrast, solar energy photocatalysis of water provides a potentially easier and economical approach to hydrogen production. Nonetheless, the efficiency of this process, particularly in converting solar energy into hydrogen, remains a significant challenge due to its insufficient light conversion rates.[29] To address these issues, researchers explored the integration of photocatalysis and electrocatalysis in PEC water splitting.[30–32] In comparison to PC, PEC generates H_2 and O_2 on separate photoelectrodes, preventing gas mixing and reversal reactions.[33] The self or external bias can mitigate charge carrier recombination in PEC, allowing for effective charge separation and migration, resulting in significantly higher efficiency compared to PC.[34]

In 1972, Fujishima and Honda pioneered PEC water splitting on a TiO_2 photoanode under ultraviolet irradiation, which has since become a cornerstone in the solar energy conversion and storage revolution.[35,36] A typical PEC system comprises a photo cathode, a photoanode, an electrolyte, and a membrane for product separation.[37] The PEC water splitting process entails two half-cell reactions: the oxygen evolution reaction (OER) on the photoanode and the hydrogen evolution reaction (HER) on the photocathode. The photocathode utilizes two electrons to produce hydrogen gas, while the photoanode employs four holes per oxygen (O_2) molecule to liberate O_2 gas. The OER is more challenging than the HER because of its higher energy barrier and slower reaction kinetics.[38,39] Consequently, developing efficient photoanode is crucial to enhance the activity of O_2 evolution and boost the efficiency for solar energy conversion in PEC water splitting.

To be an economically and commercially viable photoanode, semiconductor materials must meet several criteria simultaneously such as an appropriate band gap for sufficient absorption of visible range of solar spectrum, suitable band alignment and effective separation of charge carriers at the semiconductor/aqueous interface, low overpotential for performing water splitting half oxidation/reduction reaction, electrochemical and chemical stability, and cost-effectiveness.[40–42] In this regard, a wide range of materials based on oxides,[43–47] chalcogenides,[48–51] nitrides,[52] and phosphides[53] have been explored for water splitting processes. Among these materials,

monoclinic $BiVO_4$ stands out as a highly promising photoanode because of its suitable bandgap (2.3–2.5 eV) for absorbing visible light and advantageous band edge potential positions for efficient PEC water splitting.[54,55] Moreover, $BiVO_4$ has a high theoretical photocurrent density of 7.5 mA cm^{-2} and a STH conversion efficiency of 9.2% under AM 1.5 solar light irradiation (100 mW cm^{-2}), making it suitable for practical applications.[56] However, the unmodified $BiVO_4$ photoanode exhibits lower photocurrent densities and efficiencies than theoretically predicted.[57,58] This discrepancy can be attributed to several factors, including its short hole diffusion length, excessive electron hole recombination and slow O_2 evolution kinetics.[59] Therefore, various strategies, including morphology control,[60–62] metal or non-metal doping,[63–65] crystal facet engineering,[66,67] heterojunction construction,[68–70] and cocatalyst loading,[71–80] have been developed to enhance the PEC performance of $BiVO_4$.

Particularly, the deposition of oxygen-evolution cocatalysts (OECs) on $BiVO_4$ has been recognized as an advantageous and efficient method to enhance PEC water splitting by lowering the energy barrier, increasing active sites, and accelerating the surface OER.[80–82] Although IrO_2 and RuO_2 are now regarded as the most efficient OECs for water splitting and have been used to improve the PEC performance of $BiVO_4$, their costly price, scarcity, and insufficient stability restrict their practical application.[73,83] Therefore, there is significant interest in designing an effective photoanode comprised of potential $BiVO_4$ materials and highly efficient, low cost, non-noble-metal OER electrocatalysts.

Layered double hydroxides (LDHs) (Fig. 1) have been recognized as one of the most promising non noble metal O_2 evolution electrocatalysts due to their distinct physicochemical characteristics, and ease of synthesis in nanostructures, making them attractive for various applications, particularly in energy conversion and storage.[84–86] LDHs, also known as a hydrotalcite-like compound, are 2D layer anionic clays. The basic structure of LDH is represented as $[M_{1-x}^{2+}M_x^{3+}(OH)_2]^{x+}[A_{x/m}^{m-}\cdot nH_2O]$, where M^{2+} and M^{3+} are divalent and trivalent metals, respectively, and 'A' is the exchangeable interlayered anion.[87] Generally, LDHs exhibit a 2D nanosheet structure, which offers numerous advantages. Firstly, it enables the inclusion of a variety of metal species and the ability to change their ratios within the interlayer structure. Secondly, the large interlayer spacing of LDHs enhances the rate of ion diffusion. Furthermore, the hierarchical porosity of LDHs offers an extensive surface area and numerous active sites that facilitate charge transfer at the electrolyte interface, thereby boosting the performance of PEC systems.[88–90] Considering these collective attributes, LDHs present themselves as appealing co-catalysts for fabricating the $BiVO_4$ photoanode, which may lead to exceptional PEC performance.

Recently, several comprehensive reviews on $BiVO_4$ photoelectrodes have thoroughly explored synthesis methods and modification techniques, including morphology control, diverse nanostructures, heterostructures and cocatalyst integration. However, a detailed review focusing solely on LDHs combined with $BiVO_4$ is still lacking, thus the missing part must be addressed by discussing the latest advancements in using LDHs to enhance $BiVO_4$ photoanodes. In this review, the basic principles of PEC water splitting and the roles of LDHs are firstly summarized. Secondly, it covers the development of different composite structures, including $BiVO_4$ combined with bimetallic and trimetallic LDHs, as well as other $BiVO_4$-based composites such as $BiVO_4$/metal oxide, metal sulfide, and various charge transport layers integrated with LDHs. Additionally, LDH composites incorporating materials like graphene, carbon dots (CDs), quantum dots (QDs), single-atom catalysts, and techniques for surface engineering and LDH exfoliation with $BiVO_4$ are discussed. The design principles of these composites, with a specific focus on how LDHs enhance the performance of $BiVO_4$ by increasing efficiency and stability through synergistic effects, are also analyzed. Finally, some challenges and perspectives in future research toward developing efficient and stable $BiVO_4$/LDHs photoelectrodes for PEC water splitting are described.

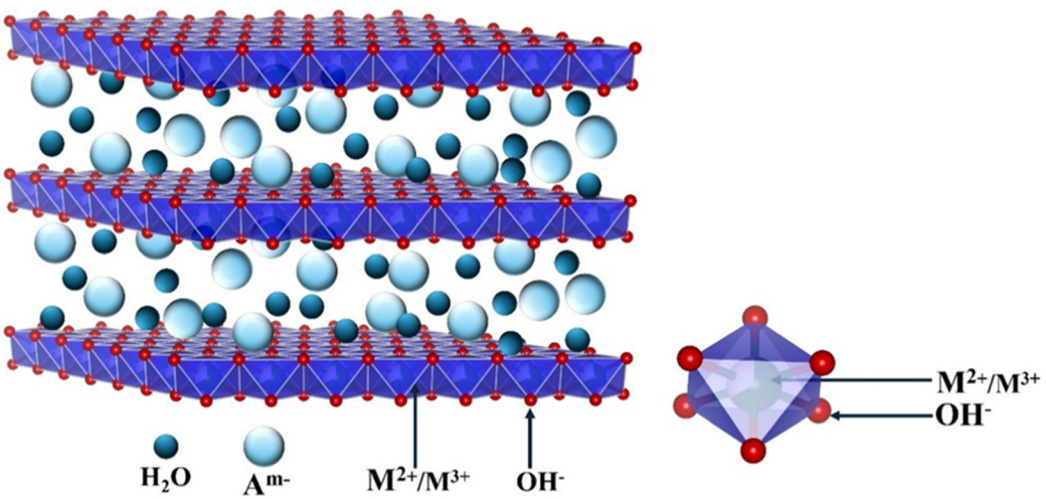

Fig. 1 Basic structure of LDH. A and M stand for anion and metal ion, respectively.

2. Principle of photoelectrochemical water splitting

PEC processes are at the forefront of renewable energy research, offering an appealing approach for converting solar energy into high-density chemical energies, notably H_2 in water splitting. Generally, a PEC cell harnesses photon energy to facilitate chemical reaction that dissociates water into H_2 and O_2 gases.[42,90,91] The PEC cell typically involves an anode and a cathode in an electrolyte, connected by an external circuit. A semiconductor photoanode is commonly employed as the working electrode, which absorbs photon energy. The cathode, usually composed of platinum (Pt), serves as the counter electrode and an external circuit is utilized to facilitate the transfer of electrons from the anode to the cathode (Fig. 2a).[92,93] In general, water splitting in the PEC reaction involves three fundamental physicochemical processes:[94] (i) the absorption of light by a semiconductor photoanode, which leads to the generation of electron–hole pairs. (ii) the separation and transportation of the photogenerated charge carriers and (iii) the water splitting reaction by the photoexcited electrons–holes at the electrode–electrolyte interface. The charge transfer mechanism at the electrode–electrolyte interface is critical for enhancing the overall PEC water splitting efficiency, as it governs the water oxidation and reduction half reactions, as shown in Fig. 2b.

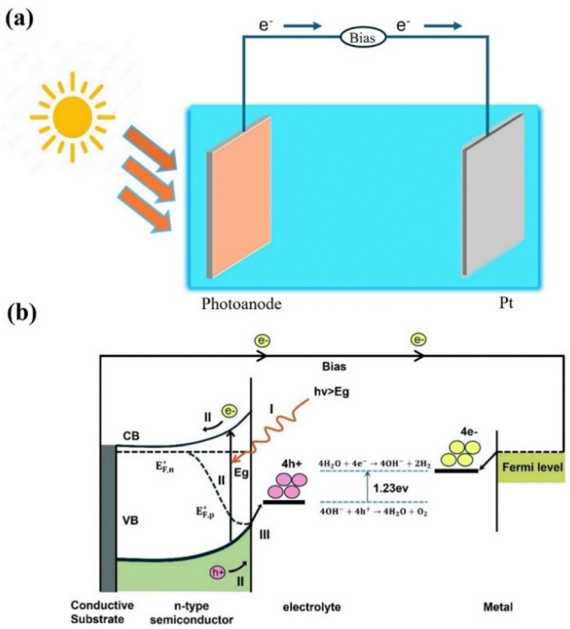

Fig. 2 (a) A schematic representation of a typical PEC water splitting cell based on photoanodes. (b) Schematic illustration of a basic PEC cell comprising an n-type semiconducting photoanode coupled with a counter electrode under an external bias. On the photoanode, $4OH^- + 4H^+ \rightarrow 2H_2O + O_2$ occurs under alkaline conditions, and a bias is necessary, as the location of the conduction band (CB) is too positive to facilitate water reduction. The basic processes are: (I) light absorption; (II) photogenerated charge carrier separation and transfer and (III) surface water splitting redox reactions. Reproduced from ref. 94, CC. BY 3.0.

When a semiconductor material is immersed in an electrolyte in the absence of light, charge (electron or hole) transfer occurs between the semiconductor and the electrolyte to align the Fermi level (EF) of the semiconductor with the redox potential (E_{Redox}) of the electrolyte.[95] This equilibration causes band bending at the semiconductor interface. The band bending generates an electric field near the semiconductor surface as a result of the disparity in electrochemical potential between the semiconductor and the electrolyte, creating a space charge layer (SCL). In this region, electrons or holes accumulate at the surface, while the bulk of the semiconductor remains electrically neutral.[96,97] Thus, the space charge layers induce an internal electric field, which plays a vital role in the separation of the photogenerated electrons and holes.[95,98,99]

When an n-type semiconductor *i.e.* photoanode is in equilibrium with E_{Redox}, band bending occurs upward, forming a positively charged depletion layer in the SCL, while a negatively charged Helmholtz layer is generated on the photoanode's surface. Similarly, when the p-type photocathode is immersed in the electrolyte, the band bends downwards.[30,100–102] Upon illumination by solar light, a semiconductor photoanode absorbs photons with energy equal to or exceeding its bandgap, generating electron–hole pairs, where excited electrons in the valence band (VB) are transferred to the conduction band (CB), resulting in holes being left in the VB. When an external bias voltage is applied, electrons migrate through the external circuit to the surface of the counter electrode, where they take part in the HER. Meanwhile the holes transfer to the photoanode surface to undergo the OER.[103,104] The water splitting reactions at the photoanode and counter electrode at different pH are as follows:[34,105]

Acidic solution:

$$\text{OER: } 2H_2O \rightarrow O_2 + 4H^+ + 4e^- \quad (E^\circ = -1.23 \text{ V } \textit{vs.} \text{ NHE})$$

$$\text{HER: } 4H^+ + 4e^- \rightarrow 2H_2 \quad (E^\circ = 0.00 \text{ V } \textit{vs.} \text{ NHE})$$

Basic solution:

$$\text{OER: } 4OH^- \rightarrow O_2 + 2H_2O + 4e^- \quad (E^\circ = -0.40 \text{ V } \textit{vs.} \text{ NHE})$$

$$\text{HER: } 4H_2O + 4e^- \rightarrow 2H_2 + 4OH^- \quad (E^\circ = -0.83 \text{ V } \textit{vs.} \text{ NHE})$$

Overall reaction

$$H_2O \rightarrow 1/2\ O_2 + H_2 \quad (\Delta G = +237.2 \text{ kJ mol}^{-1})$$

The water splitting reaction is an endothermic process that requires a Gibbs free energy of $\Delta G = 237.2$ kJ mol^{-1} to split one molecule of water into H_2 and 1/2 O_2. This energy corresponds to a photon energy of 1.23 V per electron transfer.[105] Therefore, the semiconductor photoanode must capture light radiation with photon energy exceeding 1.23 eV and utilize this energy to split water. Moreover, to effectively reduce and oxidize water, the CB edge has a more negative value than the H2 evolution potential (0 V *vs.* NHE), while the VB edge should have a more positive value than the oxygen evolution potential from water

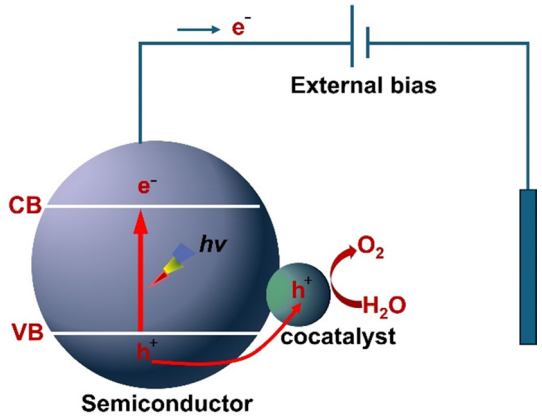

Fig. 3 A schematic illustration of the PEC mechanism in a semiconductor integrated cocatalyst.

(1.23 V *vs.* NHE).[106,107] An extra over potential is necessary to compensate for energy losses caused by the movement of photogenerated holes within the space charge region and the transfer of electrons through the external circuit to the counter electrode to drive the HER and OER reactions.[94] Hence, an ideal semiconductor photoanode is required to have an energy range of approximately 1.6 to 2.4 eV to harness solar energy for water splitting.[108,109] Photoanodes should possess excellent light absorption, rapid electron–hole separation, and minimal over potential for efficient water splitting. However, no single material has yet met these criteria. Various methods have been employed to enhance solar water splitting devices, such as applying functional cocatalysts on the surface of the electrode to provide reaction sites and catalyze the HER and OER, as shown in Fig. 3. Furthermore, the use of cocatalysts can reduce photocorrosion and improve the chemical stability of the semiconductor-based photoelectrode.[21,110–112]

3. Role of LDHs

LDHs represent a class of anionic clay materials with a brucite-like layered structure, wherein various metal cations can occupy within the octahedral sites of the layers.[113,114] Due to their structural properties, LDHs have been extensively explored in electrochemistry, photochemistry, adsorption, catalysis, and photocatalysis.[115–117] Developing visible light active photocatalyst LDHs is essential for both research and practical application. Transition metal-based oxides, hydroxides, and LDHs especially those with Fe, Co, Ni, Zn, and Mn are promising due to their affordability, ease of preparation, and high activity, offering optimal adsorption energies and enhanced catalytic performance.[118,119,120,121a,b,c,d] The unique structure, tunable composition, and remarkable physicochemical properties of LDHs, along with their ability to integrate into sophisticated molecular assemblies, enhance semiconductor photoanode performance in PEC water splitting.[122,123] Specifically, LDHs have received significant attention for their role in enhancing the performance of $BiVO_4$ photoanodes.

Fig. 4 Schematic illustration of the role of LDHs in enhancing the PEC performance of $BiVO_4$ photoanodes.

Studies have highlighted several key functions of LDHs when combined with $BiVO_4$ in PEC water oxidation reactions, as presented in Fig. 4.

3.1. Light absorption enhancement

Efficient light absorption and charge carrier generation at the photoanode/OEC interface are crucial for enhancing PEC water oxidation activity. LDHs, which can be considered as "doped semiconductors," play a significant role in promoting the visible light absorption and utilization.[124] By adjusting the ratio of metal cations in LDHs, it is possible to fine-tune their band gap and light absorption properties, thereby altering the range of light absorption and the oxidation–reduction potential.[125]

Interfacial tuning of LDHs, such as modifying the ratio of metal cations, can effectively adjust the band gap and enhance PEC performance. For example, Yang *et al.* developed a three-dimensional (3D) $BiVO_4$/Fe-based ($Ni_{1-x}Fe_x$ and $Co_{1-x}Fe_x$) LDH core/shell heterostructure film.[126] Their study revealed that the $BiVO_4/Ni_{0.5}Fe_{0.5}$-LDH photoanode exhibited a photocurrent density that was four times higher than that of bare $BiVO_4$ at 1.23 V *vs.* the reversible hydrogen electrode (RHE). Additionally, there was a cathodic shift in the onset potential of 320 mV, and the incident photon-to-current conversion efficiency (IPCE) for PEC water oxidation showed an approximate four-fold improvement compared to the bare $BiVO_4$ mainly due to the optimized light absorption by band-gap engineering.

Moreover, LDHs have been found to possess a small band gap, considerably enhancing their light-harvesting capacities.[127] For example, He *et al.* prepared a $BiVO_4$@CoAl-LDH composite.[128] The dual light-absorbing characteristics of this composite photoanode enhance its ability to capture irradiated light. Specifically, the lower bandgap CoAl-LDH (2.2 eV) absorbs longer wavelengths of visible light, while the broader bandgap $BiVO_4$ (2.4 eV) absorbs shorter ones, as confirmed by UV-vis absorption and IPCE analysis. By integrating materials with distinct bandgaps, this design

maximizes solar energy efficiency. Consequently, the $BiVO_4$@-CoAl-LDH photoanode exhibited improved PEC performance, achieving an IPCE at 400 nm that is double that of pure $BiVO_4$. This substantial improvement is due to the synergistic effect of the dual light-absorbing properties and efficient charge separation facilitated by the LDHs.

3.2. Enhanced charge transfer and separation

Loading OEC on $BiVO_4$ enhances overall PEC properties by increasing charge transfer of photogenerated holes from the semiconductor's VB to the catalyst, thereby increasing charge separation and allowing more holes to be involved in surface reactions.[129,130] LDHs, with their variable valence states of metal cations, play a critical role in this process. When photogenerated holes are produced in the semiconductor, low-valence metal cations in LDHs are oxidized to higher valence states by photogenerated holes, enhancing charge carrier transfer and separation. For instance, Guo *et al.* synthesized the Mo-$BiVO_4$/NiFe-LDH heterostructure through electrodeposition.[131] The photogenerated holes in $BiVO_4$ predominantly facilitate the oxidation of low valence Ni^{2+} to higher valence of Ni^{3+}/Ni^{4+} within NiFe-LDH, subsequently contributing to the OER, thereby enhancing the PEC performance for water decomposition. Zhong and his collaborators developed a self-healing photoanode using ultrathin (u)-CoAl-LDH on Mo:$BiVO_4$.[132] In this photoanode, u-CoAl-LDH acts as an efficient OEC. By rapidly extracting photogenerated holes through the conversion of Co^{2+} to Co^{3+} species, it significantly accelerates the proton transfer process and redirects the rate-determining step of the Mo:$BiVO_4$ photoanodes, which utilize a non-proton transfer mechanism (Fig. 5). Consequently, the charge separation efficiency is enhanced to nearly 100% on the photoanode surface and facilitates the overall PEC performance. Moreover, Huang *et al.* reported $BiVO_4$/NiFe-LDH photoanodes, where the incorporation of nanosheet NiFe-LDH significantly shortens the transfer distance of photogenerated holes at the $BiVO_4$/OER catalyst interface, thereby enhancing charge separation and photocurrent density.[133]

3.3. Suppression of charge carrier recombination

Due to lattice defects or impurities in semiconductors, materials generate surface trapping states that facilitate rapid charge carrier recombination. This leads to a significant decrease in photocurrent density of pristine semiconductor photoanodes compared to their theoretical values, thereby hindering the overall performance of PEC water splitting.[134a,b] Deposition of the electrocatalyst, such as LDHs on the surface of a $BiVO_4$ can reduce the excessive surface trapping states by facilitating interfacial hole transfer, and therefore suppress the recombination of photogenerated electron–hole pairs.[134c] In this respect, Meng and co-workers reported the deposition of NiFeV-LDH on B-$BiVO_4$. The author suggested that the main factor restricting the photocurrent density of $BiVO_4$ materials is severe surface charge recombination, as demonstrated using intensity modulated photocurrent spectroscopy (IMPS).[135] They found that after decorating $BiVO_4$ photoanodes with a NiFeV-LDH, the PEC performance of the $BiVO_4$ photoanodes was significantly enhanced due to the efficient suppression of charge recombination.

Moreover, Mane *et al.* developed a surface oxygen vacancy-incorporated (O_{vac}):$BiVO_4$/NiFe-LDH photoanode,[136a] in which the NiFe-LDH transport layer extracts holes from the valence band of $BiVO_4$:O_{vac}. This configuration enhances charge transport to the electrolyte, reduces surface trapping states, and promotes the participation of more energetic holes in the water-oxidation reaction. During this process, high-valence Ni species (Ni^{3+}/Ni^{4+}) are reduced to Ni^{2+}, which minimizes charge recombination and completes the catalytic cycle (Fig. 6). Consequently, the excellent charge transfer ability of the O_{vac}:-$BiVO_4$/NiFe-LDH photoanode enhances PEC performance for water oxidation. Furthermore, clarifying the function of cocatalysts in suppressing surface charge recombination and enhancing catalytic activity contributes to the observed photocurrent improvements in semiconductor/electrocatalyst processes. Lin and Boettcher highlighted the importance of adaptive junctions at interfaces of these materials, where permeable electrocatalysts allow electrolyte access.[111,136b] The junctions modify the barrier height and band bending according to the cocatalyst's oxidation state and the applied bias, leading to increased photovoltage and enhanced charge transfer dynamics. This concept applies specifically to the deposition of catalysts on the photoanode surface, where the junction

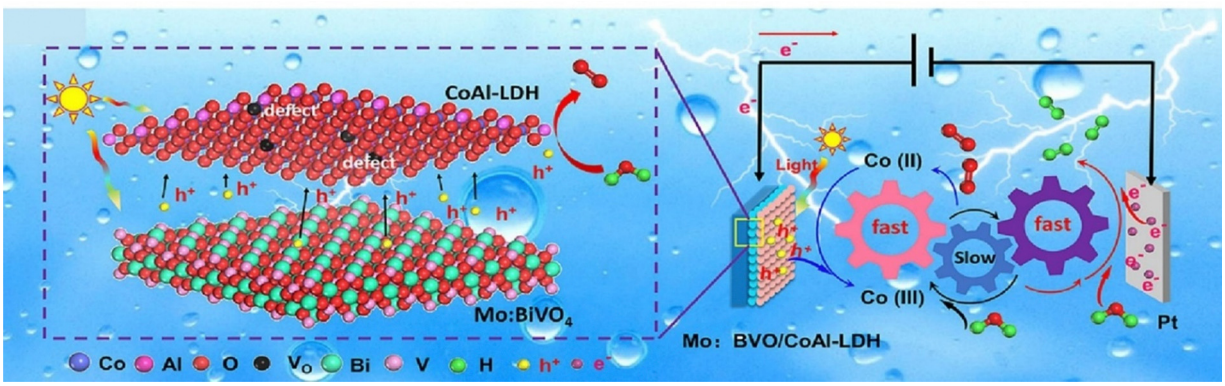

Fig. 5 Schematic representation of PEC water splitting utilizing Mo:$BiVO_4$/u-COAl-LDH. Reproduced with permission from ref. 132, Copyright 2023, Elsevier.

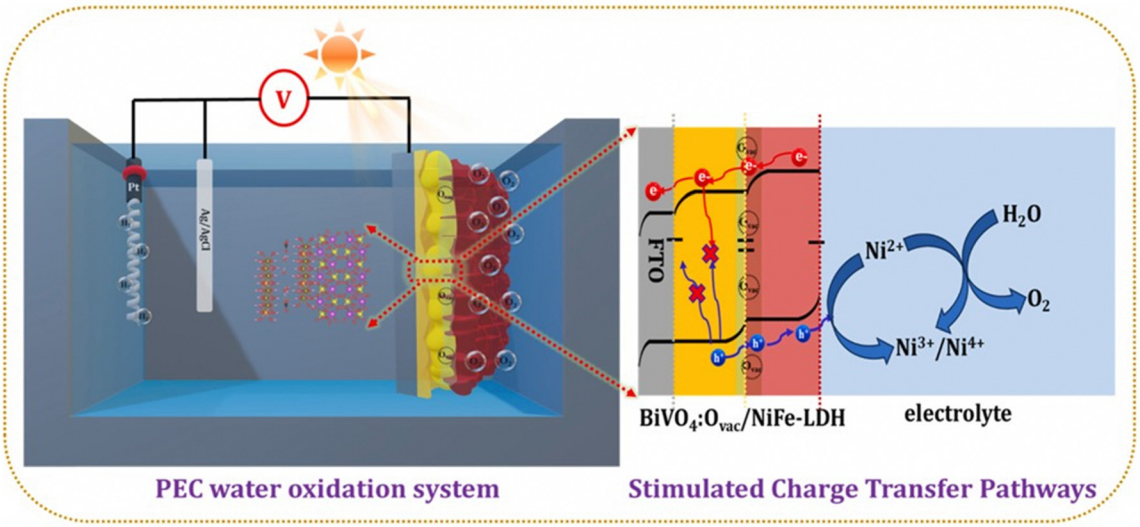

Fig. 6 A schematic illustration of the process for the enhanced charge transport pathway in the O_{vac}:$BiVO_4$/NiFe-LDH photoanode for PEC water oxidation. Reproduced with permission from ref. 136*a*, Copyright 2024, Elsevier.

type is significantly influenced by the deposition method. In this regard, Chhetri *et al.* effectively utilized pulse plating to electrodeposit amorphous $CoLa(OH)_x$ mixed double hydroxide onto nanoporous $BiVO_4$, achieving precise controlled layer of thickness and enhanced adhesion, resulting in a favorable $BiVO_4$/MDH interface.[136c] This adaptive interface effectively suppresses photogenerated charge recombination and improves charge transport through grain size regulation, leading to a significant enhancement in PEC performance.

3.4. Enhancement of water oxidation activity

Due to the high overpotential and sluggish water oxidation kinetics, a large number of photogenerated charge carriers tend to recombine on the $BiVO_4$ photoanode surface. This recombination significantly reduces the photocurrent density and lowers the reactivity of the photoanode.[137–139] Loading OECs such as LDHs is an effective strategy to enhance the reactivity of the photoanode. For instance, Zhao *et al.* prepared a $BiVO_4$/CoMn photoanode for efficient PEC water splitting.[140] After loading the CoMn-LDH cocatalyst, the photocurrent density increased sharply, reaching 2.45 times that of the pristine $BiVO_4$ photoanode. This considerable improvement suggests that decorating CoMn-LDH nanoflakes provides high-valence state active sites [$Co^{3+\delta}/Mn^{3+\delta}$ $(0 < \delta < 1)$] for water oxidation, by oxidizing Co^{2+}/Mn^{2+} in the LDH nanoflakes through holes. Subsequently, the $Co^{3+\delta}/Mn^{3+\delta}$ ions can be reversibly reduced to their original Co^{2+}/Mn^{2+} state, as shown in Fig. 7a. This continuous cyclic activity enhances the hole transport and lowers the overpotential, thereby boosting the PEC water oxidation reaction.

Moreover, Vo *et al.* reported a $BiVO_4$/CoMnZn photoanode prepared *via* an electrodeposition method.[141] The primary cause of the catalytic activity in the OER is generally due to the presence of Co and Mn, whilst Zn plays a role in providing structural support and enabling cooperative effects. When the ternary CoMnZn-LDH is coupled with $BiVO_4$, the M^{2+}(Co, Mn) ions accept photogenerated holes from the VB of $BiVO_4$ and undergo oxidation to form high-valence active sites (M^{3+} or M^{4+}) due to their lower formation energy barrier. Subsequently, these ions with high valence levels undergo oxidation of H_2O to produce O_2 while reverting back to their initial valence state (Fig. 7b and c). This process enhances the rate at which interfacial holes are extracted from the surface of the photoelectrode, hence improving the overall water splitting efficiency.

3.5. Enhancements of stability under water oxidation

One of the most critical factors for the practical application of photoanodes in PEC is stability. However, the photostability of $BiVO_4$-based photoanodes remains a significant challenge to achieving substantial PEC water splitting due to the tendency of V^{5+} ions in $BiVO_4$ to dissolve in harsh electrolyte environments under solar radiation.[142] Loading a cocatalyst layer to $BiVO_4$ effectively inhibits the dissolution of V^{5+} from the $BiVO_4$ lattice, enhances charge transfer rate, and inhibits photocorrosion.[143–145] However, the ultra-thin cocatalyst layer is not consistently stable due to changes in the structure during operation and the loss of catalyst materials resulting from agitation and dissolution.[146a,b] The deposition of catalysts on photoanodes *via* spray pyrolysis is now being considered a simpler and more scalable method, facilitating precise control over layer structure and ensuring strong adhesion to substrates to address this issue.[146c] Meanwhile, LDHs manufactured through the hydrothermal approach demonstrate high particle purity, favorable distribution, ideal crystal shape, and excellent controllability.[146d]

For instance, Wang *et al.* prepared an oxygen vacancy-incorporated $BiVO_4$/(O_{vac})-NiFe-LDH photoanode *via* a hydrothermal method,[146e] demonstrating that the LDH acts as a hole-shuttling mediator for oxygen evolution. Loading O_{vac}-NiFe-LDH on $BiVO_4$ greatly improves the photoanodes' charge separation and injection efficiency. As a result, the $BiVO_4$/(O_{vac})-NiFe-LDH photoanode showed exceptional stability for 80 h in a V^{5+} ion

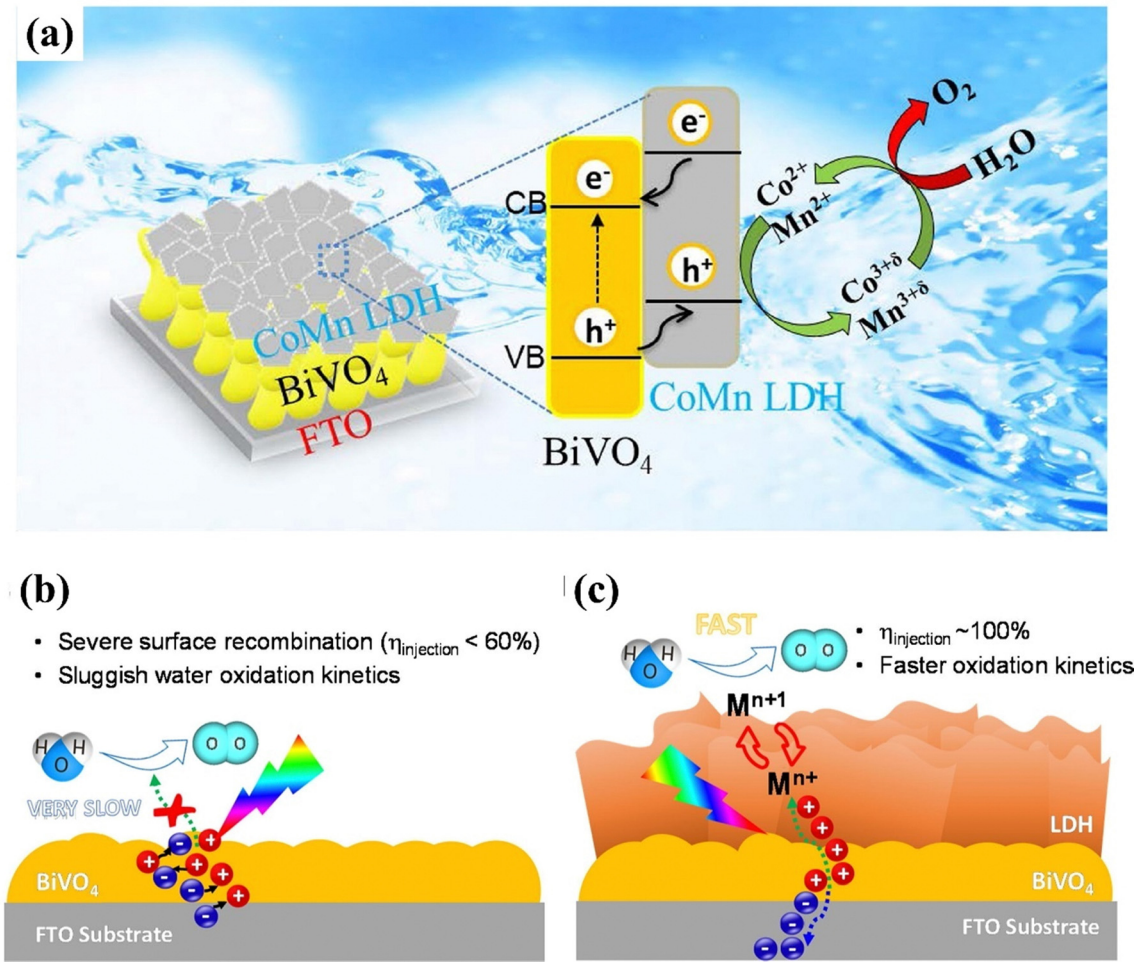

Fig. 7 (a) Schematic representation of PEC water splitting utilizing the $BiVO_4$/CoMn-LDH photoanode. Reproduced with permission from ref. 140, Copyright 2020, Elsevier; (b) and (c) Illustrative depiction of charge carrier dynamics during water oxidation on $BiVO_4$ and $BiVO_4$/CMZ-LDH photoelectrode. Reproduced with permission from ref. 141, Copyright 2019 Elsevier.

saturated borate buffer electrolyte, as shown in Fig. 8a. He and his coworkers reported the synthesis of a NiFeY-LDH cocatalyst on $BiVO_4$,[147] where the inclusion of Y altered the chemical surroundings of Ni, resulting in a decrease in surface charge recombination. This modification led to a highly functional $BiVO_4$/NiFeY-LDH photoanode that exhibited a substantial PEC performance and outstanding stability of approximately 25 h (Fig. 8b).

3.6. Improvement of surface wettability

Wettability pertains to the extent of compatibility and affinity between a heterogeneous catalyst and liquid reactants. Surface roughness and micro-morphology have a significant impact on the surface wettability of semiconductor materials.[148,149] A photoanode with a hydrophilic surface enhances water molecule adsorption and facilitates gas separation, hence enhancing the overall efficiency of PEC water splitting.[150] For example, Yue *et al.* prepared a super-hydrophilic $BiVO_4$/CoAl-LDH photoanode.[151] This photoanode exhibited an impressive photocurrent density of 3.5 mA cm^{-2} at 1.23 *vs.* RHE, about 3.2 times higher than that of the bare $BiVO_4$ photoanode, with a negative shift in onset potential of 0.30 V. The improved water oxidation capability is ascribed to the well-matched energy level between LDH and $BiVO_4$, along with the engineered surface wettability. As illustrated in Fig. 9(a–i), the surface morphology of the $BiVO_4$/CoAl-LDH photoanode is characterized by nanosheets. After plasma treatment, the thickness of $BiVO_4$/H-CoAl-LDH is drastically reduced while its morphology remains unchanged. Moreover, $BiVO_4$ and $BiVO_4$/CoAl-LDH materials exhibit hydrophilic properties with contact angles of 27.75° and 46.84°, respectively. In contrast, H-CoAl-LDH/$BiVO_4$ demonstrates exceptional superhydrophilicity, with a contact angle of 2.87°. The superhydrophilic surface of H-CoAl-LDH/$BiVO_4$ accelerates the adsorption of water molecules on surface active sites, leading to outstanding surface reaction activity and enhanced PEC water oxidation efficiency.

4. Recent advancement of $BiVO_4$ and LDH for PEC water oxidation

In this chapter, $BiVO_4$/bimetallic-LDH, $BiVO_4$/trimetallic-LDH, $BiVO_4$ composites/LDH, and $BiVO_4$/LDH composites are reviewed

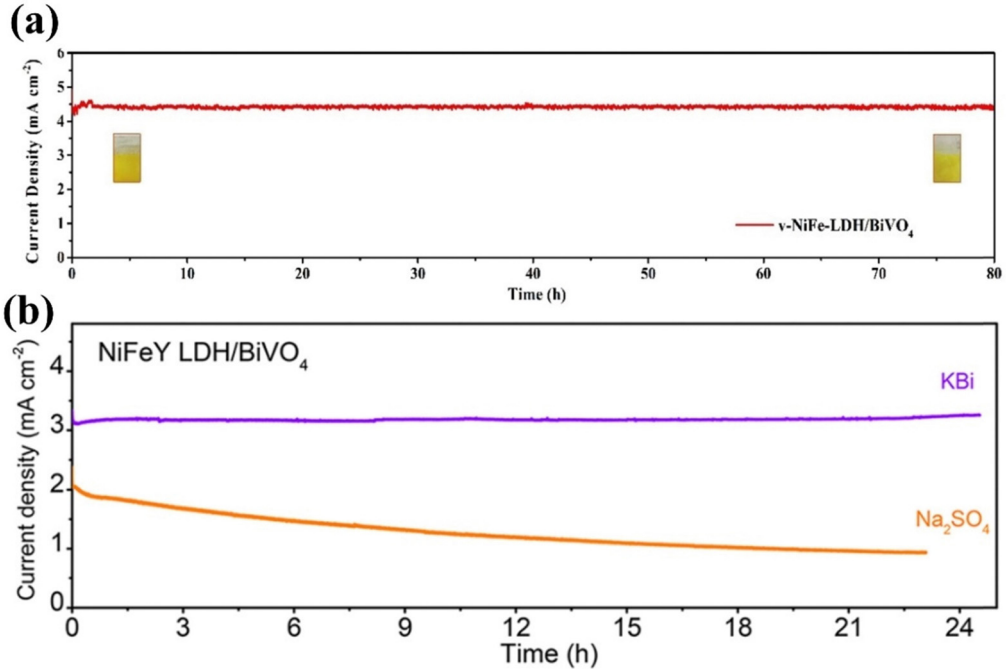

Fig. 8 (a) Current *vs.* time curve of $BiVO_4$/v-NiFe-LDH in KB + V at 1.23 V_{RHE} over 80 h. Reproduced with permission from ref. 146*e*, Copyright 2023, American Chemical Society. (b) Current–time profiles of $BiVO_4$/NiFeY-LDH in 1 M KBi (pH = 9) and 0.2 M Na_2SO_4 (pH = 7) at 0.8 V_{RHE} for around 24 h. Reproduced with permission from ref. 147, Copyright 2020, American Chemical Society.

and discussed to understand the relationship between their structure, properties, and PEC water splitting performance. Relevant research from 2015 to 2024 on $BiVO_4$/LDH photoanodes for PEC water splitting is listed in Table 1.

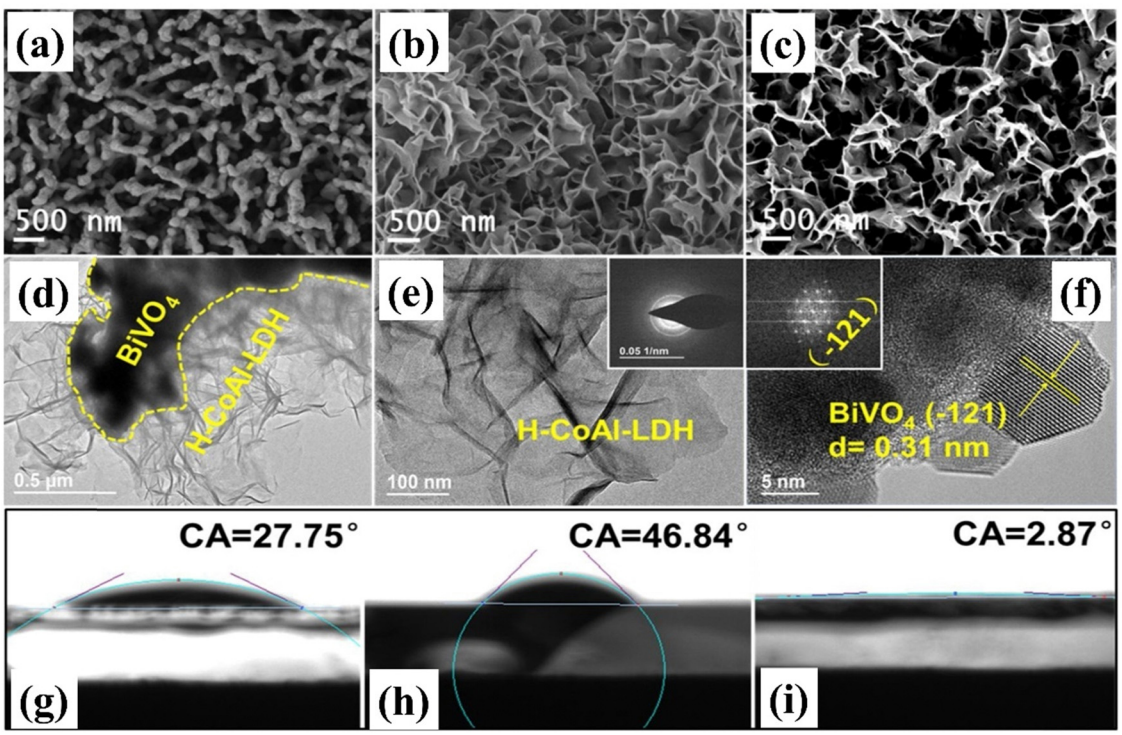

Fig. 9 SEM images of (a) $BiVO_4$, (b) $BiVO_4$/CoAl-LDH, and (c) $BiVO_4$/H-CoAl-LDH, and TEM and HTEM images of $BiVO_4$/H-CoAl-LDH (d)–(f), inset in (e): diffraction ring, inset in (f): diffraction pattern; contact angle $BiVO_4$ (g), $BiVO_4$/CoAl-LDH (h) and $BiVO_4$/H-CoAl-LDH (i) electrodes. Reproduced with permission from ref. 151, Copyright 2021, Elsevier.

Table 1 Recent progress of the $BiVO_4$/LDH photoanode for PEC water splitting

Photoanode	Synthesis	Morphology	Electrolyte	Light source	Applied bias	Photocurrent (mA cm^{-2})	Stability (h)	Ref.	Publication year
$BiVO_4$/Bimetallic LDH									
$BiVO_4$/NiFe-LDH	Hydrothermal	Nanoparticles	0.5 M Na_2SO_4	Light emitting diode lamp (CEL-LED100)	0.6 V *vs.* Ag/AgCl	2.49	3	152	2018
$BiVO_4$/NiFe LDH	Hydrothermal	Nanosheet	0.1 M $KHCO_3$ (pH = 8.6)	AM 1.5 solar simulator	1.23 V *vs.* RHE	4.45	30	133	2017
$BiVO_4$/NiFe-LDH	Electrodeposition	—	0.5 M Na_2SO_4	AM 1.5 (100 mW cm^{-2}) illuminator	1.23 V *vs.* RHE	1.21	12	126	2017
$BiVO_4$/NiCo-LDH	Electrodeposition	Nanoparticle	0.5 M Na_2SO_4 (pH = 7.3)	AM 1.5 solar simulator	1.23 V *vs.* RHE	3.4	2	73	2020
Nd: $BiVO_4$/NiCo-LDH	Hydrothermal	Nanosheet	0.5 M Na_2SO_4 (pH = 6.8)	AM 1.5 solar simulator (100 mW cm^{-2})	1.23 V *vs.* RHE	4.1	3	153	2024
$BiVO_4$/NiMn-LDH	Hydrothermal	Nanosheet	0.5 M Na_2SO_4	500 W xenon lamp	1.23 V *vs.* RHE	0.83	0.5	154	2019
$BiVO_4$@CoAl-LDH	Hydrothermal	Nanosheets	0.1 M PBS (pH = 7), 0.1 M H_2O_2	300 W xenon lamp	1.23 V *vs.* RHE	1.0	—	128	2015
$BiVO_4$/CoMn-LDH	Electrodeposition	Nanoflake	0.5 M Kpi	AM 1.5 solar simulator	1.23 V *vs.* RHE	2.69	2.7	140	2020
$BiVO_4$/CoFe-LDH	Chemical bath deposition	Nanoparticle	0.5 M KBi (pH = 9.2)	100 mW cm^{-2} simulated sun light	1.23 V *vs.* RHE	4.3	1	155	2022
$BiVO_4$·O_{vac}/NiFe-LDH	Electrodeposition	Nanosheet	0.5 M Na_2SO_4	300 W xenon arc lamp	1.23 V *vs.* RHE	2.92	20	136	2024
Mo: $BiVO_4$/NiFe-LDH	Electrodeposition	Nanosheet	0.1 M Na_2SO_4 (pH = 7)	AM 1.5 solar simulator (100 mW cm^{-2})	1.23 V *vs.* RHE	1.58	2.2	131	2019
Fe-$BiVO_4$/CoFe-LDH	Electrodeposition	Nanoparticle	0.3 M K_2SO_4, 0.2 M PBS	500 W xenon lamp	1.23 V *vs.* RHE	2.56	5	156	2024
$BiVO_4$/CE-NiFe-LDH	Cation exchange		0.5 M Na_2SO_4	150 W xenon lamp	1.23 V *vs.* RHE	4.03	10	157	2021
$BiVO_4$/Trimetallic LDH									
$BiVO_4$/ZnCoV-LDH	Electrodeposition	Nanosheet	0.1 M NaBi (pH = 9.4)	500 W xenon arc lamp	1.23 V *vs.* RHE	2.55	2	158	2020
$BiVO_4$/CoMnZn-LDH	Electrodeposition	Nanosheet	0.1 M NaBi (pH = 9.4)	AM 1.5 solar simulator	1.23 V *vs.* RHE	1.06		141	2019
$BiVO_4$/ZnCoFe-LDH	Electrodeposition	Nanolayer	1 M Na_2SO_3	AM 1.5 solar simulator	1.23 V *vs.* RHE	3.43	2.7	159	2021
$BiVO_4$/NiCoV-LDH	Electrodeposition	Nanosheet	0.1 M KPi (pH = 7)	AM 1.5 xenon lamp (100 mW cm^{-2})	1.23 V *vs.* RHE	3.32		160	2024
B-$BiVO_4$/NiFeV-LDH	Hydrothermal, drop casting	Nanosheet	1 M KBi (pH = 9.3), 0.2 M Na_2SO_3	100 W xenon arc lamp	1.23 V *vs.* RHE	4.6	24	135	2021
$BiVO_4$/Y-NiFe-LDH	Hydrothermal	Nanosheet	1 M KBi (pH = 9.5), 0.2 M Na_2SO_4	AM 1.5 xenon lamp (100 mW cm^{-2})	1.23 V *vs.* RHE	5.2	25	147	2020
$BiVO_4$ Composites/LDH									
WO_3/$BiVO_4$/NiCo-LDH	Hydrothermal	Nanosheet	0.5 M Na_2SO_4 (pH = 6.9)	150 W xenon lamp	1.23 V *vs.* RHE	3.2	2	161	2024
Fe_2O_3/$BiVO_4$/NiFe-LDH	Electrodeposition	Nanosheets	1 M NaOH (pH = 13.16)	300 W xenon lamp	1.8 V *vs.* RHE	1.7	—	162	2018
WO_3/$BiVO_4$/NiFe-LDH	Electrodeposition	Nanoparticle	0.5 M Na_2SO_4 (pH = 7.0)	300 W xenon lamp	1.23 V *vs.* RHE	1.78	24	163	2023
TiO_2/$BiVO_4$/NiFe-LDH	Hydrothermal	Nanoparticle	0.05 M Na_2SO_4	500 W xenon lamp	0.8 V *vs.* RHE	0.017	0.55	164	2019
WO_3-$BiVO_4$-NiFeCr-LDH	Electrodeposition	Nanosheet	0.1 M PBS (pH = 6.9)	AM 1.5G solar lamp	1.23 V *vs.* RHE	4.9	6	165	2021
MoO_3/$BiVO_4$/CoMnZn-LDH	Electrodeposition	Nanosheet	0.1 M Na_2SO_4	500 W xenon lamp	1.23 V *vs.* RHE	1.24	1	166	2020
$BiVO_4$/CdS/NiCo-LDH	Electrodeposition	Nanosheets	0.5 M Na_2SO_3 (pH = 7)	—	1.23 V *vs.* RHE	2.72	1	167	2019
$BiVO_4$/CdS/NiFe-LDH	Electrodeposition	Nanosheet	0.5 M Na_2SO_4	300 W xenon lamp	1.23 V *vs.* RHE	3.1	3	168	2024
$BiVO_4$/MoO_x/NiFe-LDH	Electrodeposition	Nanosheet	0.1 M KBi (pH = 9)	100 mW cm^{-2}	1.23 V *vs.* RHE	2.7	0.069	169	2022
$BiVO_4$/MoO_3/CoMn-LDH	Electrodeposition	Nanosheet	1 M KBi (pH = 9)	300 W xenon lamp, AM 1.5 solar light (100 mW cm^{-2})	1.23 V *vs.* RHE	3.78	2	170	2023
$BiVO_4$/$CuFeO_2$/NiFe-LDH	Electrodeposition	Nanosheet	1 M Na_2SO_4	300 W xenon arc lamp	1.23 V *vs.* RHE	4.34	5	171	2022
$BiVO_4$/$CuCoO_2$/$NiCo_3$-LDH	Electrodeposition	Nanosheet	0.5 M Na_2SO_4	xenon lamp (100 mW cm^{-2})	1.8 V *vs.* RHE	6.95	2	172	2023
$BiVO_4$/BNNPs/CoCr-LDH	Hydrothermal	—	0.1 M Na_2SO_4 (pH = 6)	1.5 G filter (100 mW cm^{-2})	1.23 V *vs.* RHE	3.8	3	173	2022
$BiVO_4$/FeOOH/ZnFe-LDH	Electrodeposition	Thin plates	1 M Na_2SO_4 (pH = 7)	300 W xenon arc lamp	1.23 V *vs.* RHE	4.92	1.66	174	2022
$BiVO_4$/CuPc/NiCo-LDH	Hydrothermal	Nanosheet	0.5 M KBi (pH = 9.5)	300 W solar simulator (AM 1.5 solar light)	1.23 V *vs.* RHE	4.03	15	175	2022
$BiVO_4$/P_3HT-CuPc/NiCo-LDH	Hydrothermal	Nanosheet	0.5 M KBi (pH = 9.5)	300 W solar simulator (AM 1.5 solar light)	1.23 V *vs.* RHE	4.25	8	176	2022
$BiVO_4$/rGO/NiFe-LDH	Electrodeposition	Nanoarrays	0.5 M Na_2SO_4 (pH = 6.9)	150 W xenon lamp	1.23 V *vs.* RHE	1.30	10	177	2018
$BiVO_4$/rGO/NiFe-LDH	Electrodeposition	Nanosheets	Kpi (pH = 7)	300 W xenon lamp	1.23 V *vs.* RHE	1.13		178	2019

Table 1 (*continued*)

Photoanode	Synthesis	Morphology	Electrolyte	Light source	Applied bias	Photocurrent ($mA\ cm^{-2}$)	Stability (h)	Ref.	Publication year
$BiVO_4$/GQDs/CoSn-LDH	Hydrothermal	Thin layer	0.1 M KBi (pH = 11)	300 W Tungsten halogen lamp	1.23 V *vs.* RHE	4.15	4	179	2021
$BiVO_4$/rGO/NiFe-LDH	electrodeposition	Nanoplates	1 M KBi (pH = 9.33)	150 W xenon lamp, AM 1.5 solar light	1.23 V *vs.* RHE	3.26	1	180	2020
$BiVO_4$/Au@SiO_2/CoAl-LDH	Hydrothermal	Nanosheet	0.1 M PBS (pH = 7)	300 W xenon lamp	1.23 V *vs.* RHE	1.92	2	181	2018
OH-$BiVO_4$@C@NiFe-LDH	Electrodeposition	—	0.5 M KBi (pH = 9.3)	AM 1.5 (100 mW cm^{-2})	1.23 V *vs.* RHE	5.31	20	182	2024
$BiVO_4$/AgAuNCs/CoNi-LDH	Electrodeposition	Nanosheets	0.5 M Na_2SO_4 (pH = 7)	AM 1.5 (100 mW cm^{-2})	1.23 V *vs.* RHE	3.75	2.77	183	2024
$BiVO_4$/LDH Composites									
$BiVO_4$/CoAl-LDH/Graphene	Hydrothermal	Nanosheet	Kpi (pH = 7)	300 W xenon arc lamp	1.23 V *vs.* RHE	2.13	—	75	2017
$BiVO_4$/NiFe-LDH/CQD	Electrodeposition	Nanosheets	0.5 M PBS (pH = 7)	300 W xenon arc lamp	1.23 V *vs.* RHE	2.84	3	184	2018
$BiVO_4$/CoAl/CdTeQD	Hydrothermal	Nanosheet	0.1 M PBS (pH = 7)	300 W xenon lamp, AM 1.5 solar light (100 mW cm^{-2})	1.23 V *vs.* RHE	2.23	4	185	2016
$BiVO_4$@NiFe-LDHs/Ru	Electrodeposition	Nanosheet	0.5 M KBi, 0.2 M Na_2SO_3	300 W xenon lamp	1.23 V *vs.* RHE	4.65	5	186	2024
$BiVO_4$/CoFe-Ac LDH/SAsPt	Hydrothermal	—	1 M KBi	AM 1.5 xenon lamp (100 mW cm^{-2})	1.23 V *vs.* RHE	5.14	20	187	2023
$BiVO_4$/H-CoAl-LDH	Hydrothermal, plasma etching	Nanosheet	0.5 M Na_2SO_4	AM 1.5 solar light	1.23 V *vs.* RHE	3.5	3	151	2021
Mo: $BiVO_4$/u-CoAl-LDH	Coprecipitation, dipping coating	Nanosheet	KBi (pH = 9.5)	AM 1.5 xenon lamp (100 mW cm^{-2})	1.23 V *vs.* RHE	5.8	1.38	132	2023
$BiVO_4$/O_{vac}NiFe-LDH	Hydrothermal	—	0.5 M K_3BO_3 (pH= 9.5)	AM 1.5 xenon lamp (100 mW cm^{-2})	1.23 V *vs.* RHE	5.81	80	146	2023
$BiVO_4$/HD-NiCo-LDH	Drop casting	Nanosheet	0.5 M Na_2SO_4 (pH = 7)	xenon lamp, AM 1.5 (100 mW cm^{-2})	1.23 V *vs.* RHE	4.54	—	188	2024

4.1. $BiVO_4$/bimetallic LDHs

LDHs are multi-metal anionic clays having metal cations embedded into the octahedral sites of their layers.[113,114,189] LDHs containing transition metals such as Co, Fe, Mn, and Ni have recently been recognized as efficient PEC water oxidation catalysts.[190] Incorporating other transition metal elements into monometallic hydroxides such as $Ni(OH)_2$ and $Co(OH)_2$ is a versatile approach to enhance their intrinsic electrocatalytic activity. This bimetallic incorporation increases the number of active sites and modifies the electronic structure of the original metal hydroxides.[191–194] Due to their efficient oxygen evolution activity, loading bimetallic LDHs onto $BiVO_4$ is an effective approach to increase its PEC water splitting performance. For instance, Wang *et al.* studied Ni-based bimetallic NiFe-LDH on $BiVO_4$ using a one-step hydrothermal process.[152] HRTEM images of the NiFe-LDH/$BiVO_4$ photoanode (Fig. 10a) revealed interplanar distances of approximately 0.363 and 0.318 nm, corresponding to the (511) and (421) planes, respectively, of the NiFe-LDH nanoparticles. The results demonstrated that NiFe-LDH nanoparticles enhance the visible light absorption through reflection and scattering, leading to a substantial enhancement in the PEC characteristics of $BiVO_4$. Consequently, the $BiVO_4$/NiFe-LDH photoanode achieved the highest photocurrent density of 2.49 mA cm^{-2} at 0.6 V *vs.* Ag/AgCl, indicating an increase of 217% and a factor of 2.5 compared to bare $BiVO_4$. Furthermore, it exceeds by 3.07 and 1.25 times, of $BiVO_4$/$Ni(OH)_2$ (0.81 mA cm^{-2}) and $BiVO_4$/$Fe(OH)_2$ (1.98 mA cm^{-2}) photoanodes (Fig. 10b) and demonstrated superior onset potentials and stability.

Similarly, Huang and his coworkers fabricated a $BiVO_4$/NiFe-LDH photoanode, incorporating NiFe-LDH nanosheet arrays as the OEC to facilitate charge separation and enhance surface reaction kinetics.[133] This design resulted in a photocurrent density of 4.02 mA cm^{-2} at 1.23 V *vs.* RHE, representing a 2.8-fold increase compared to that of pristine $BiVO_4$. The photoanode demonstrated an impressive, applied bias photon-to-current efficiency (ABPE) of 1.07% at 0.75 V *vs.* RHE and showcased a notable O_2 evolution rate of 29.6 μmol h^{-1} cm^{-2}, maintaining high activity for more than 30 h in a weak $KHCO_3$ alkaline electrolyte.

Mane *et al.* incorporated surficial oxygen vacancies onto $BiVO_4$ and developed the O_{vac}:$BiVO_4$/NiFe-LDH photoanode.[136] The introduction of oxygen vacancies effectively adapts band energetics, improves light absorption, and elevates carrier density. The 2D-NiFe-LDH nanosheets act as a proficient hole transport layer at the electrode/electrolyte interface and provide photocorrosion protection. The O_{vac}:$BiVO_4$/NiFe-LDH photoanode exhibited a photocurrent density of 2.92 mA cm^{-2}, reflecting a 3-fold improvement over the pristine $BiVO_4$. The extensive stability testing demonstrated that the combined impact of these efficacious strategies lead to a 91% retention of the photocurrent density of the O_{vac}: $BiVO_4$/NiFe-LDH photoanode following 20 h of irradiation, as depicted in Fig. 10c.

Guo *et al.* prepared a Mo:$BiVO_4$/NiFe-LDH photoanode for PEC water splitting.[131] The incorporation of Mo into the $BiVO_4$ lattice enhances its visible light capabilities and elevates carrier concentration. In this design, the Ni component effectively captures photo-generated holes to facilitate the oxidation of

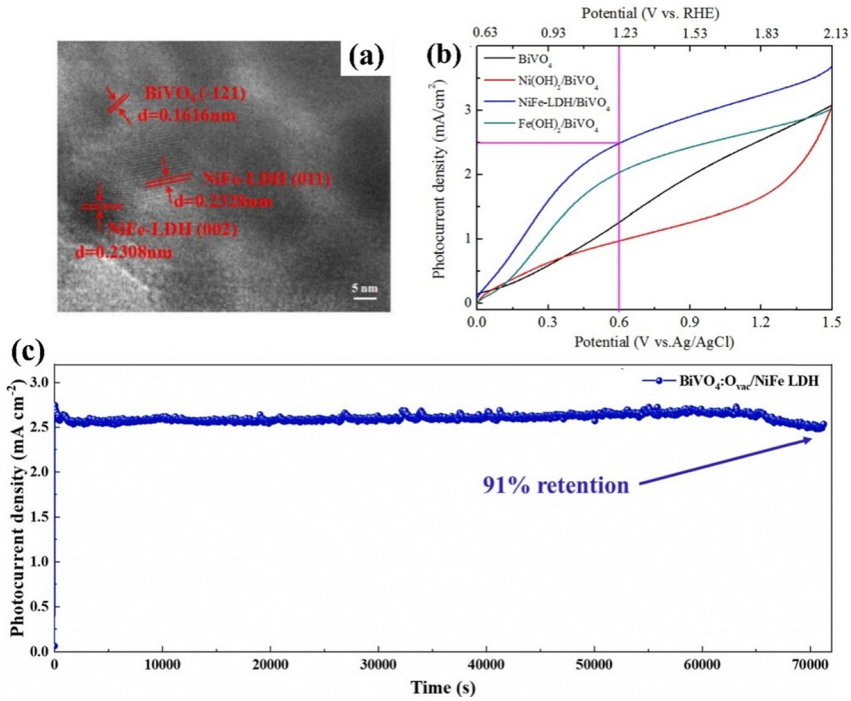

Fig. 10 (a) HRTEM of the $BiVO_4$/NiFe- LDH photoanode, (b) current–voltage curves of $BiVO_4$, $BiVO_4$/$Ni(OH)_2$, $BiVO_4$/$Fe(OH)_2$, and $BiVO_4$-LDH/$BiVO_4$ photoanodes under visible light illumination. Reproduced with permission from ref. 152, Copyright 2020, Elsevier. (c) Stability test for the O_{vac}:$BiVO_4$/NiFe-LDH photoanode. Reproduced with permission from ref. 136, Copyright 2024, Elsevier.

low-valence Ni^{2+} into high-valence Ni^{3+} and Ni^{4+} within the potential range of 0.6 to 1.6 V *vs.* RHE (Fig. 11a). The $BiV_{0.97}Mo_{0.03}O_4$/NiFe-LDH photoanode exhibited a 64%incident photon-to-current efficiency (Fig. 11b), surpassing the 10% IPCE of undoped $BiVO_4$, along with a significant shift in the onset potential and enhanced stability. The photocurrent density $BiV_{0.97}Mo_{0.03}O_4$/NiFe-LDH photoanode showed 1.58 mA cm^{-2} at 1.23 V *vs.* RHE, which is 1.25 times and 3.16 times higher than that of $BiV_{0.97}Mo_{0.03}O_4$ and pure $BiVO_4$.

Moreover, She *et al.* constructed a $BiVO_4$/NiCo-LDH using electrodeposition.[73] This heterojunction structure significantly improved light absorption and electron–hole separation, resulting in a photocurrent of 3.4 mA cm^{-2} at 1.23 V *vs.* RHE, surpassing that of the bare $BiVO_4$ (1.1 mA cm^{-2}).

Wang *et al.* developed a photoanode consisting of Nd:$BiVO_4$ and NiCo-LDH cocatalyst.[153] The inclusion of Nd greatly increases the carrier density and lowers the charge transfer resistance, which improves the $BiVO_4$ photoanode's electrical conductivity. The NiCo-LDH catalyst works as a bifunctional OER co-catalyst, with Co improving hole extraction and Ni increasing active sites, thus enhancing PEC water oxidation activity. Consequently, the Nd: $BiVO_4$/NiCo-LDH photoanode showed a photocurrent density of 4.1 mA cm^{-2} at 1.23 V *vs.* RHE (Fig. 11c), indicating an enhancement of approximately 5.1 times relative to the unmodified $BiVO_4$, with a negative shift in onset potential of 399 mV.

Zhang and colleagues designed a pyramidal-shaped $BiVO_4$/NiMn-LDH composite photoanode using a one-step hydrothermal method.[154] The compatibility of the energy level between $BiVO_4$ and NiMn-LDH facilitates hole transport from $BiVO_4$'s valence band to NiMn-LDH. Therefore, NiMn-LDH captured h^+ through M^{2+}/M^{3+} to generate M^{3+}/M^{4+} (M = Ni, Mn). By promoting hole collection and injections, this process reduces charge carrier recombination in the $BiVO_4$/NiMn-LDH composite photoanode relative to bare $BiVO_4$, leading to enhanced OER efficiency. Consequently, the $BiVO_4$/NiMn-LDH photoanode showed an optimal photocurrent of 0.83 mA cm^{-2} at 1.23 V *vs.* RHE, which is two times higher than that of bare $BiVO_4$. Moreover, the onset potential of the $BiVO_4$/NiMn-LDH photoanode showed a cathodic shift around 480 mV.

Wei *et al.* investigated the role of CoFe-LDH as an oxygen cocatalyst for PEC-water splitting on $BiVO_4$.[155] They reported two types of LDHs: crystalline CoFe-LDH (C), which was deposited on $BiVO_4$ using a low-temperature chemical bath method, and amorphous CoFe-LDH (E) coatings that were achieved through electrodeposition. The amorphous CoFe-LDH (E) layer primarily acted as a "shunt channel," instead of participating in the water oxidation reaction. In contrast, the crystalline CoFe-LDH effectively disrupted the "shunt channel" between the cocatalyst and the FTO substrate, thereby inhibiting the recombination of photogenerated charges. Moreover, the interface between the crystalline CoFe-LDH (C) and $BiVO_4$ exhibited fewer surface trap states than the amorphous layer. The $BiVO_4$/CoFe-LDH (C) photoanodes achieved a photocurrent of 4.3 mA cm^{-2} at 1.23 V *vs.* RHE, with an ABPE% of 1.2% at 1.01 V, which is 1.5 times higher than that of the amorphous $BiVO_4$/CoFe-LDH (E) and four times higher than that of bare $BiVO_4$.

He *et al.* synthesized a $BiVO_4$/CoAl-LDH photoanode using a hydrothermal method for water oxidation.[128] The investigation found that the CoAl-LDH nanosheet formed interconnected

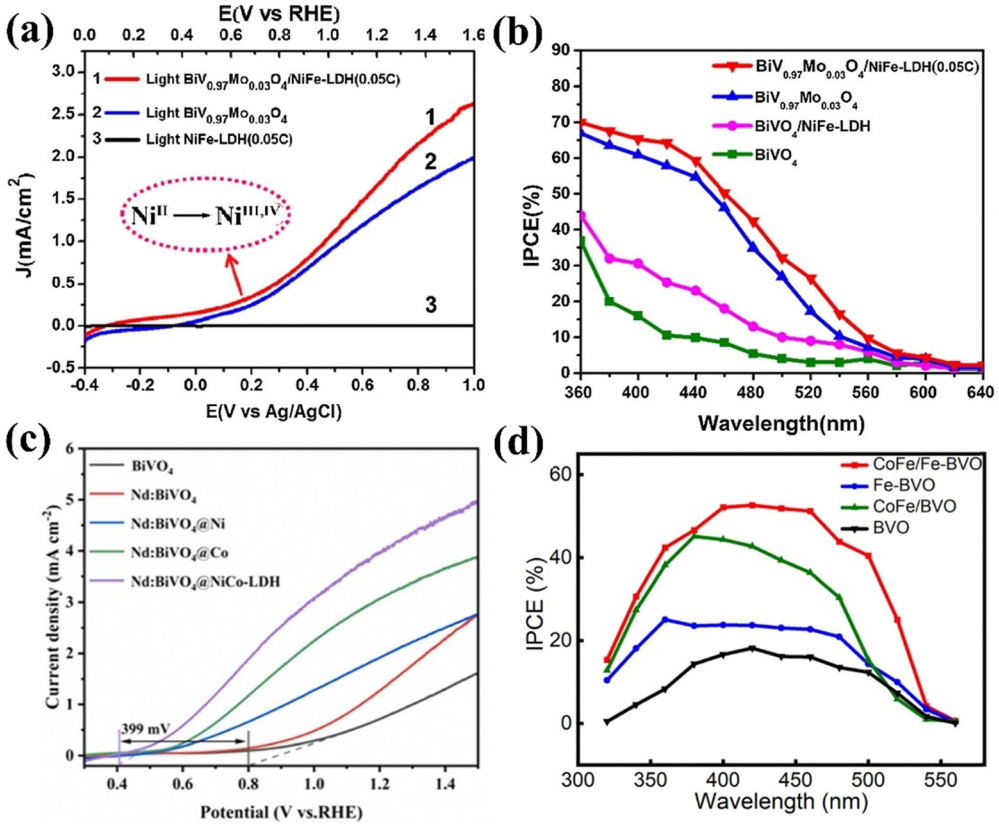

Fig. 11 (a) Photocurrent density of the $BiV_{0.97}Mo_{0.03}O_4$/NiFe-LDH [0.05C(Coulomb)] photoanode, (b) IPCE of $BiVO_4$, $BiV_{0.97}Mo_{0.03}O_4$ and $BiV_{0.97}Mo_{0.03}O_4$/NiFe-LDH (0.05C) photoanodes. Reproduced with permission from ref. 131, Copyright 2019, Elsevier. (c) Linear sweep voltammetry (LSV) curves for the Nd:$BiVO_4$@NiCo-LDH photoanode. Reproduced with permission from ref. 153, Copyright 2024, Elsevier. (d) Photoconversion efficiency of monochromatic incident light based on wavelength. Reproduced with permission from ref. 156, Copyright 2024, American Chemical Society.

nanowalls with a thickness of 20 nm, resulting in more active sites and enhanced carrier-transporting capabilities, allowing holes to diffuse to the photoanode's surface. Consequently, the $BiVO_4$/CoAl-LDH photoanode exhibited a 540 mV cathodic shift in onset potential and a photocurrent density of 1.0 mA cm^{-2} at 1.23 V.

Recently, Fe-$BiVO_4$/CoFe-LDH was designed by Chen *et al.* for PEC water splitting.[156] In this study, CoFe-LDH promotes carrier utilization and suppresses electron–hole recombination, whereas iron doping facilitates charge separation and transfer. The CoFe/Fe-$BiVO_4$ photoanode displayed a photocurrent of 2.56 mA cm^{-2} at 1.23 V *vs.* RHE and an IPCE of 52.1% at 400 nm, representing a 270% increase in photocurrent and a 2.2-fold enhancement in IPCE over bare $BiVO_4$ (Fig. 11d). Furthermore, the surface charge transport efficiency increased from 16.8% to 62.5% at 1.23 V *vs.* RHE.

4.2. $BiVO_4$/trimetallic LDH

Due to the high tunability in LDH composition, various active centers can be readily integrated into their structure, enabling precise regulation of active species and the electronic configuration of LDH.[195–197] Consequently, many bimetallic LDHs have exhibited considerable catalytic activity towards the OER. Nevertheless, many of the bimetallic LDHs still suffer from low electrical conductivity.[198–202] This limitation can be addressed through third-metal doping, which regulates the electronic configurations of pristine LDHs and enhances the synergistic interactions between doped and host metals, resulting in trimetallic LDHs with superior electrocatalytic performance.[203] Despite the difficulty in selection of elemental combination mainly based on the ionic radii, recent research has revealed that LDHs comprising three different transition metals demonstrate higher charge-carrier transportation and improved electronic conductivity. For example, Vo and coworkers designed a novel ZnCoV-LDH and decorated it on a $BiVO_4$ photoanode using electrodeposition.[158] Fig. 12(a–d) demonstrate that the introduction of V^{5+} ions caused the binding energy of Co 2p to shift by 1.2 eV to a higher level, indicating that Co is in an electron-deficient state. Consequently, the Co^{3+}/Co^{2+} ratio is higher in ZnCoV-LDH compared to ZnCo-LDH. Additionally, it was indicated that the partial electron transfer from Co to V is facilitated by oxygen bridges. Furthermore, the binding energy of the surface hydroxyl (OH^-) groups shifts to the left, suggesting a stronger adsorption affinity of OH^- to the metal sites. These observations suggest that ZnCoV-LDH facilitates the rapid movement of photogenerated holes from $BiVO_4$ to the ZnCoV-LDH layer on the outside. As a result, the ZnCoV-LDH/$BiVO_4$ photoanode demonstrated a 370 mV cathodic shift in onset potential and achieved a photocurrent density of 2.7 mA cm^{-2} at 1.23 V *vs.* RHE, representing a fourfold increase compared to unmodified $BiVO_4$.

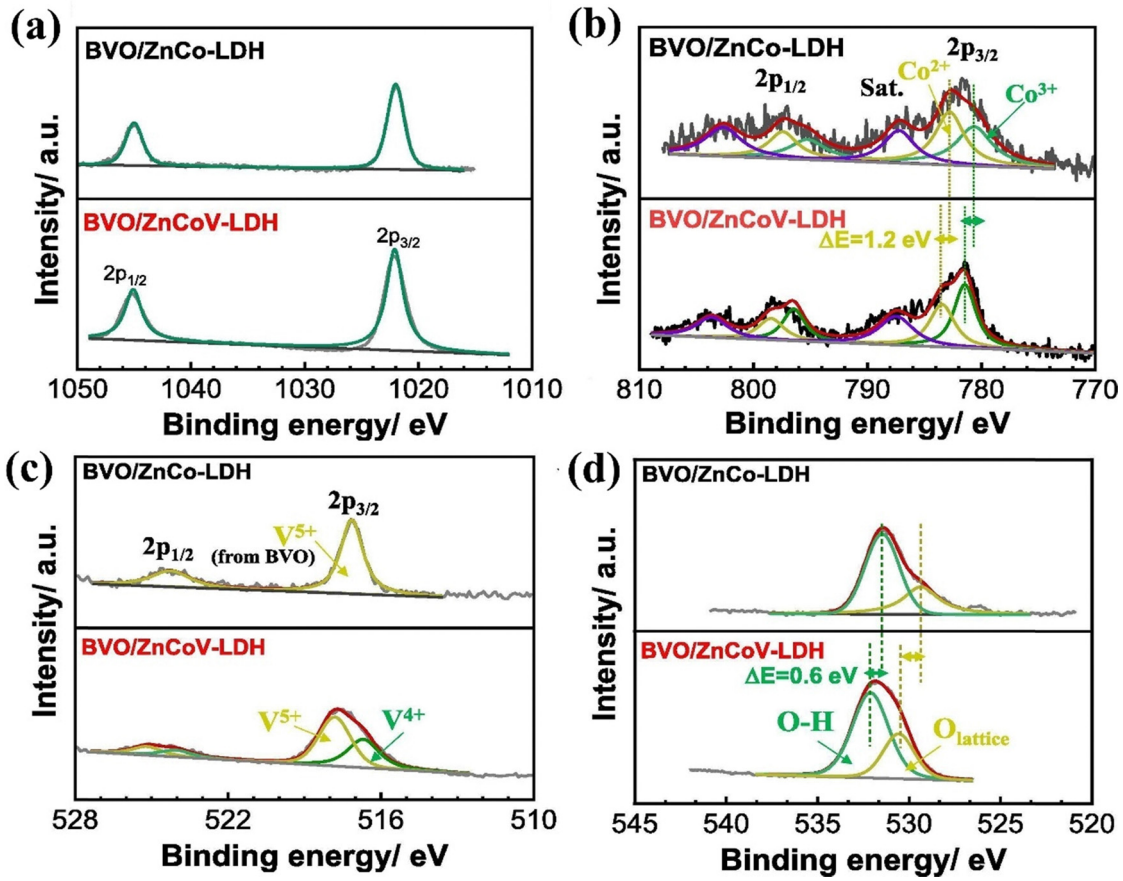

Fig. 12 High resolution XPS analysis of (a) Zn 2p, (b) Co 2p, (c) V 2p, and (d) O 1s regions of ZnCo-LDH and ZnCoV-LDH on $BiVO_4$/ZnCoV-LDH. Reproduced with permission from ref. 158, Copyright 2020, Elsevier.

The same authors fabricated $BiVO_4$/CoMnZn LDH by the electrodeposition method as well.[141] The modification of CMZ-LDH on $BiVO_4$ is confirmed by XRD through the observation of a weak (003) reflection. Six Raman peaks were observed at approximately 127, 212, 329, 368, 709, and 827 cm^{-1}, corresponding to the distinctive vibrational modes of scheelite monoclinic $BiVO_4$. Additional peaks observed at around 475 and 520 cm^{-1} were ascribed to the bending mode of O–M–O (where M denotes Co, Mn, and Zn), as illustrated in Fig. 13(a and b). In this study, CMZ-LDH acts as a cocatalyst, lowering the onset potential, enhancing the photocurrent, and serving as a protective layer for $BiVO_4$. Consequently, the composite photoanode exhibited a photocurrent density of 1.06 mA cm^{-2}, which is 1.7 times higher than that of the bare $BiVO_4$. Moreover, the deposition of CMZ-LDH on the $BiVO_4$ photoanode induced a significant cathodic shift of 280 mV in the onset potential for PEC water oxidation, suggesting effective band bending. This is evident from the change in the open circuit photovoltage (OCP). As shown in Fig. 13c, the BVO_4/CMZ-LDH photoanode exhibits a higher OCP in comparison to the bare $BiVO_4$ photoanode, indicating better charge separation due to larger band bending and hence improved PEC performance.

Meng *et al.* prepared $BiVO_4$/NiFeV LDH *via* a hydrothermal method, where NiFeV LDH served as both a water oxidation electrocatalyst and a hole reservoir, thereby reducing surface charge recombination and improving interfacial charge transfer.[135] Consequently, the NiFeV/B-$BiVO_4$ photoanode showcased an outstanding photostability, a minimal onset potential of around 0.2 V *vs.* RHE, and a photocurrent density of 4.6 mA cm^{-2} at 1.23 V *vs.* RHE.

He *et al.* designed $BiVO_4$/NiFeY LDH using a hydrothermal method.[147] The XPS and density functional theory simulation demonstrated that the incorporation of Y into Ni sites promotes efficient charge transfer between Ni and Fe by tuning the local electronic environment of the NiFe LDH, as depicted in Fig. 14(a and b). This significantly increases the transfer rate of electrons and holes at the interface of the photocatalyst. Hence, NiFeY LDH reduces interface charge recombination between $BiVO_4$ and the cocatalyst, preventing the photocorrosion of $BiVO_4$. The optimized $BiVO_4$/NiFeYLDH, as depicted in Fig. 14c, exhibited an onset potential of 0.31 V_{RHE} and a photocurrent density of 5.2 mA cm^{-2} at 1.23 V_{RHE}, surpassing the performance of $BiVO_4$/NiFeLDH (3.2 mA cm^{-2}).

Wen *et al.* constructed a $BiVO_4$/ZnCoFe-LDH photoanode by conformally decorating a ZnCoFe-LDH on a porous $BiVO_4$ photoanode using an electrodeposition method.[159] The p–n heterojunction formed between ZnCoFe-LDH and $BiVO_4$ enhances the transfer and separation of photogenerated

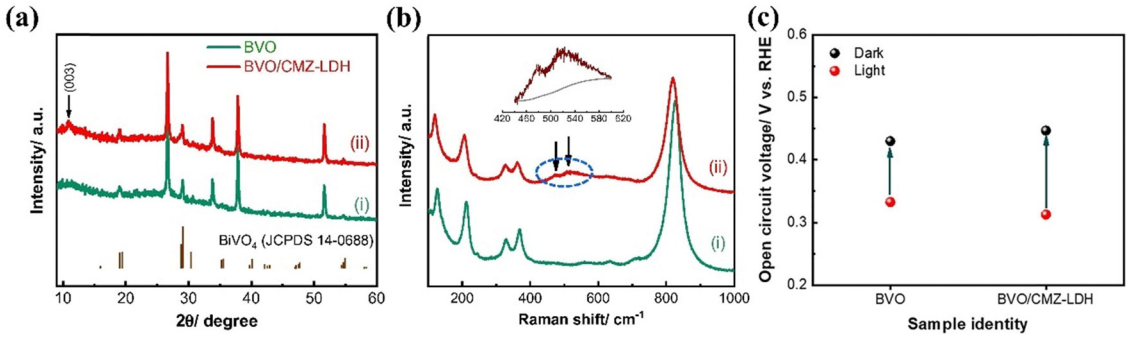

Fig. 13 (a) XRD patterns, (b) Raman spectra, and (c) open circuit configurations of the $BiVO_4$/CMZ-LDH photoanode. Reproduced with permission from ref. 141, Copyright 2019, Elsevier.

charges, extends light absorption capabilities, and facilitates the kinetics of surface water oxidation. Consequently, the $BiVO_4$/ZnCoFe-LDH photoanode exhibited a photocurrent density of 3.43 mA cm^{-2} at 1.23 V *vs.* RHE, representing a threefold increase compared to the bare $BiVO_4$ photoanode. (Fig. 14d). It also demonstrated a notable negative shift in the onset potential from 0.51 V to 0.21 V *vs.* RHE (Fig. 14e), suggesting improved cocatalytic performance and a higher rate of surface OER.

Recently Huang *et al.* developed a ternary NiCoV-LDH nanosheet on a $BiVO_4$ photoanode using a low-bias voltage electrodeposition process.[160] The SEM images revealed that LDH deposition at −0.1 V resulted in unique crystalline and amorphous structures, providing more active sites. The XRD peaks of $BiVO_4$ correspond to monoclinic bismuth vanadate (JCPDS No. 14–0688), and the peaks at 13.0° and 23.9° conform to the lattice planes of NiCoV-LDH, as depicted in Fig. 15(a–c). In this study, the introduction of vanadium (V^{5+}) elements created strong electronic interactions with Ni and Co, facilitating the transformation of Co^{2+} into Co^{3+} with enhanced catalytic activity. Simultaneously, V^{5+} was reduced to V^{3+}, increasing the sample's conductivity (Fig. 15d). Thus, $BiVO_4$/NiCoV-LDH nanosheets effectively facilitated carrier transfer at the semiconductor/electrolyte interface. Consequently, the $BiVO_4$/NiCoV-LDH photoanode demonstrated a significant increase in photocurrent density, reaching 3.32 mA cm^{-2} at 1.23 V *vs.* RHE, a 2.84-fold increase compared to pristine $BiVO_4$. It was also 1.59 and 1.25 times greater than those of the $BiVO_4$/NiCo-LDH photoanodes prepared at −0.1 V and −0.7 V without the introduction of V elements, respectively. Additionally, the surface efficiency of $BiVO_4$/NiCoV-LDH reached 71%, representing a 2.45-fold improvement over the bare $BiVO_4$.

4.3. $BiVO_4$ composites/LDHs

The N-type $BiVO_4$ semiconductor is regarded as a potential photoanode material for water splitting because of its appropriate

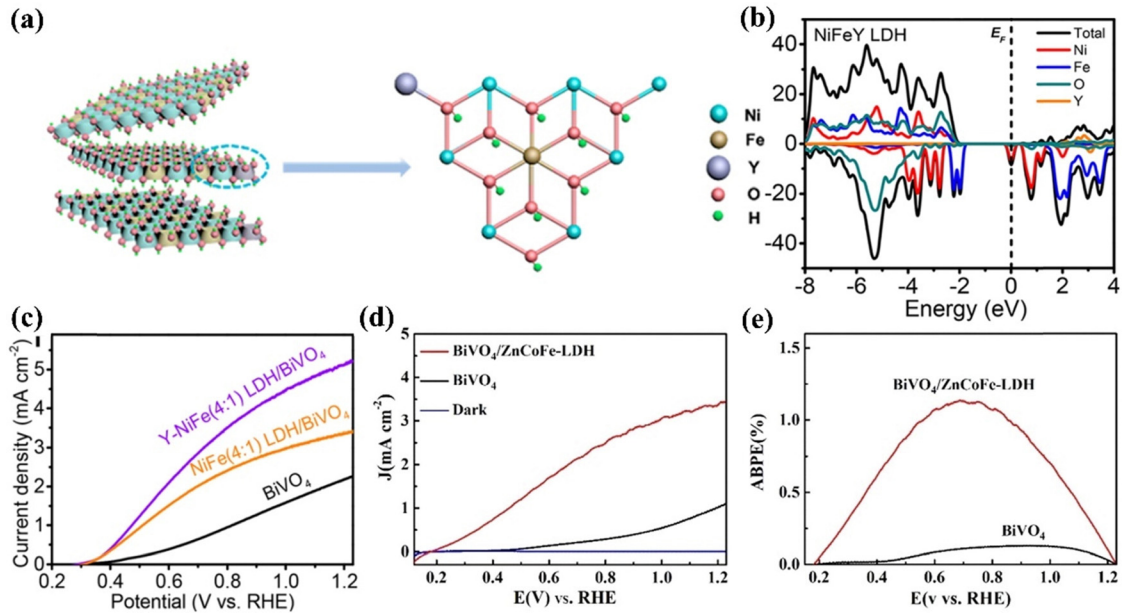

Fig. 14 (a) Structure model and (b) DFT-based DOS spectra of NiFeY LDH and (c) LSV curves of the $BiVO_4$/NiFeY photoelectrode under illumination. Reproduced with permission from ref. 147, Copyright 2020, American Chemical Society. (d) *J*–*V* curves of the $BiVO_4$/ZnCoFe-LDH photoanode (e) ABPE curves of the bare $BiVO_4$ and $BiVO_4$/ZnCoFe-LDH photoanodes. Reproduced with permission from ref. 159, Copyright 2021, Wiley-VCH GmbH.

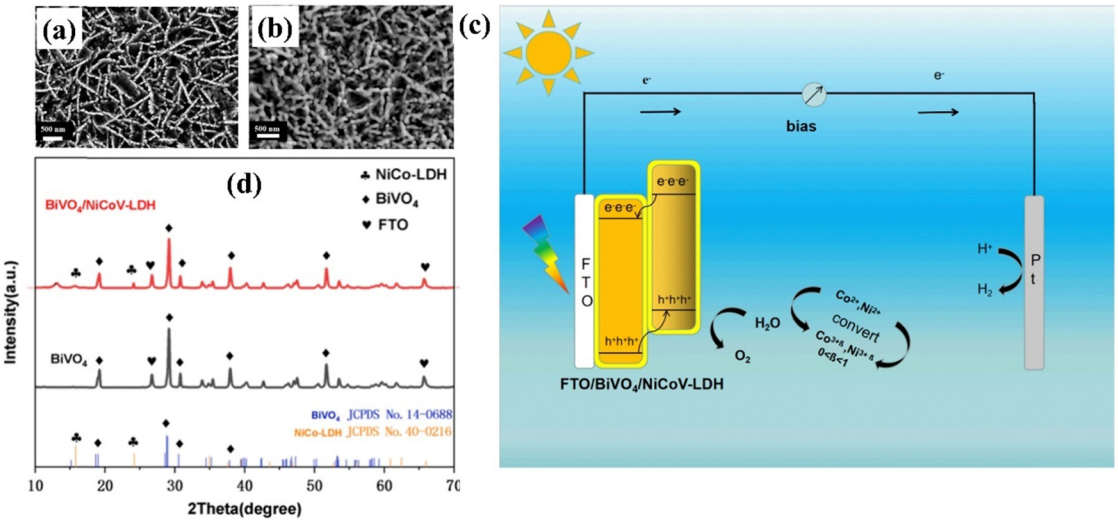

Fig. 15 (a) and (b) SEM images and (d) XRD patterns of $BiVO_4$/NiCoV-LDH. (c) Water splitting mechanism of the $BiVO_4$/NiCoV-LDH photoelectrode. Reproduced with permission from ref. 160, Copyright 2024, American Chemical Society.

band alignment and high theoretical conversion efficiency of up to 9.1%. However, it suffers from severe charge carrier recombination due to its low carrier mobility (0.044 cm V^{-1} s^{-1}) and insufficient water oxidation kinetics.[204,205] Several approaches have been employed to improve its PEC properties, including integrating $BiVO_4$ with different semiconductor metal oxides or sulfides, or decorating $BiVO_4$ with rGO, HTL, and QD to create p–n or n–n heterojunction composites.[206–210] Nevertheless, the impact of semiconductor heterojunctions is restricted by the saturation of the built-in electric field, which results from charge accumulation during the water oxidation process.[211] Therefore, an efficient and cost-effective cocatalyst is required to expedite the water oxidation reaction, since the OER at the anode remains a significant hurdle for efficient solar PEC water splitting. LDHs have emerged as a promising class of OECs because of their affordability and compatibility with semiconductor materials. LDHs containing elements such as Ni, Mn, Co, and Fe have been proven to be proficient electrochemical catalysts.[119,120,121b,c,d] In the past few years, researchers have devoted significant efforts to the development of $BiVO_4$ heterojunction composites/LDHs to improve the overall PEC water splitting performance of the $BiVO_4$ photoanode.

4.3.1. $BiVO_4$/metal oxide semiconductor/LDHs. Coupling LDHs and a metal oxide heterojunction with an n-type $BiVO_4$ photoanode has received significant attention due to their high light absorption capacity, superior carrier transfer efficiency, and excellent water oxidation kinetics. For instance, Kang *et al.* developed a $BiVO_4$/MoO_x/NiFe-LDH photoanode for PEC water splitting by incorporating MoO_x and NiFe-LDH on $BiVO_4$ *via* the electrodeposition method.[169] In this setup, MoO_x functioned as both a charge transport layer and a passivation layer, reducing surface defect states, allowing more charge transfer to the interface of MoO_x and NiFe-LDH. The NiFe-LDH significantly improved the accumulated hole consumption rate on the photoanode surface by converting low-valence Ni^{2+} and Fe^{2+} oxides into high-valence Ni^{3+}, Ni^{4+}, and Fe^{3+}, enhanced PEC water oxidation, as shown in Fig. 16. This resulted in a photocurrent density of 2.7 mA cm^{-2} at 1.23 V *vs.* RHE for the $BiVO_4$/MoO_x/NiFe-LDH photoanode, which is 3.9 times superior to that of pristine $BiVO_4$. Additionally, a more negative onset potential shift of 267 mV was observed, along with an impressive incident IPCE of 52.8% at 420 nm and ABPE of 1.03% at 0.63 V_{RHE}.

Li *et al.* constructed a $BiVO_4$/MoO_3/CoMn-LDH photoanode using electrodeposition and calcination.[170] The MoO_3/$BiVO_4$ heterojunction facilitates efficient carrier transfer and inhibits charge recombination, while CoMn-LDH boosts OER kinetics and visible light absorption. Their combined effect greatly increases charge separation and light harvesting in the $BiVO_4$/MoO_3/CoMn-LDH photoanode, reached a photocurrent density of 3.78 mA cm^{-2} at 1.23 V *vs.* RHE. This value is 1.26 and 3.78 times greater than those of $BiVO_4$/MoO_3 and pure $BiVO_4$, respectively.

LDHs and p-type semiconductor metal oxides were deposited on an n-type $BiVO_4$ photoanode surface, resulting in enhanced surface catalytic efficiency and improved separation of charge carriers. For example, Yin *et al.* created a $BiVO_4$/$CuFeO_2$/NiFe-LDH photoanode by incorporating $CuFeO_2$ and NiFe-LDH onto $BiVO_4$ *via* electrodeposition.[171] The ultra-thin p-type $CuFeO_2$ layer was introduced at the interface of $BiVO_4$ to create a p–n heterojunction that promotes charge transfer, while NiFe-LDH served as an OEC to extract holes and convert OH^- from the electrolyte into O_2, providing active sites for water oxidation. Hence, the efficiency of the PEC water splitting of the $BiVO_4$ photoanode was improved by the synergistic effects of $CuFeO_2$ and NiFe-LDH, which effectively prevented charge recombination, as shown in Fig. 17. The $BiVO_4$/$CuFeO_2$/NiFe-LDH photoanode demonstrated a photocurrent density of 4.34 mA cm^{-2} at 1.23 V *vs.* RHE, which is 3.78-fold superior to that of bare $BiVO_4$. Additionally, ABPE was 2.48%, representing an increase of 5.28 times compared to that of pristine $BiVO_4$.

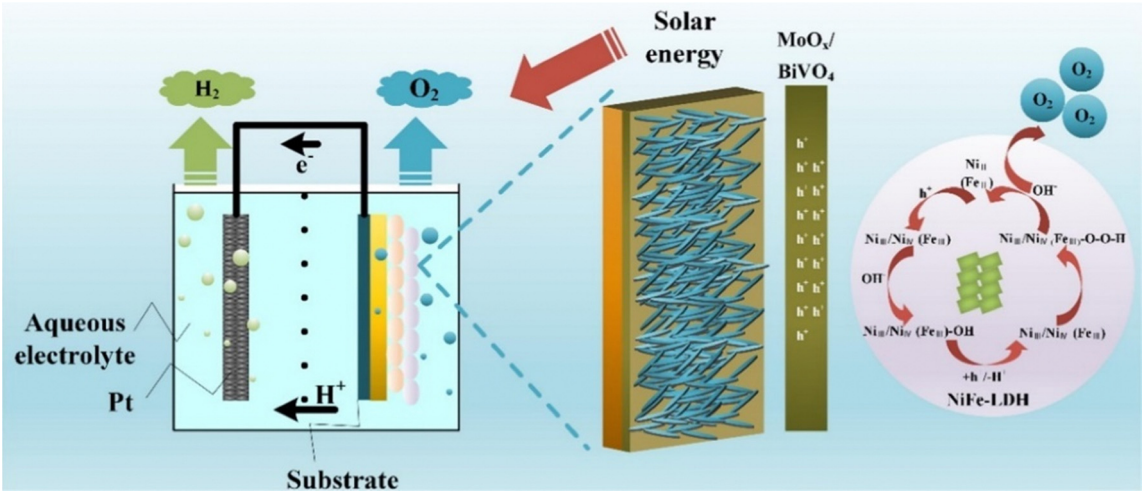

Fig. 16 Water splitting mechanism of the optimized $BiVO_4$/MoOx/NiFe photoelectrode. Reproduced with permission from ref. 169, Copyright 2022, Elsevier.

Zhang *et al.* prepared $BiVO_4$/$CuCoO_2$/$NiCo_3$-LDH for PEC water splitting, where $NiCo_3$-LDH was incorporated into $BiVO_4$/$CuCoO_2$ *via* electrodeposition to act as an OEC.[172] Consequently, the photocurrent density of $BiVO_4$/$CuCoO_2$/$NiCo_3$-LDH reached 6.95 mA cm^{-2} at 1.8 V *vs.* RHE, representing an increase of around 24.8 times compared to $BiVO_4$ and 5.5 times greater than that of $BiVO_4$/$CuCoO_2$. Additionally, it demonstrated good stability, maintaining 70% of its performance after 2 h of operation.

4.3.2. $BiVO_4$/metal sulfide semiconductor/LDHs. Metal sulfide semiconductors like CdS (band gap of 2.25 eV) are good at collecting sunlight. It has a sufficiently negative CB edge that makes it easier for photoexcited electrons to flow toward $BiVO_4$, enhancing charge separation in the $BiVO_4$/CdS heterojunction.[167] Integrating LDHs with CdS-sensitized $BiVO_4$ heterojunctions offers a promising approach for improving the PEC performance of $BiVO_4$ under visible light irradiation. For instance, the $BiVO_4$/CdS/NiCo-LDH photoanode was created by Bai *et al.* by electrodepositing NiCo-LDH onto a CdS/$BiVO_4$ substrate.[212] In this design, the CdS nanoparticles create an n–n semiconductor heterojunction with $BiVO_4$, which helps reduce charge carrier recombination by directing charge flow. NiCo-LDH acts as an efficient hole collector, facilitating the hole transport gathered at the CdS/electrolyte interface, thereby improving water oxidation under applied potential (Fig. 18a). As a result, the triadic $BiVO_4$/CdS/NiCo-LDH photoanode achieved a photocurrent density of 2.72 mA cm^{-2} (Fig. 18b), which is 1.2 times superior to $BiVO_4$/CdS and 3.6 times greater than that of bare $BiVO_4$. Additionally, it exhibited a cathodic shift in onset potential of 450 mV.

Recently, Dong *et al.* fabricated a triadic $BiVO_4$/CdS/NiFe-LDH photoanode, by sequentially depositing CdS nanoparticles and NiFe-LDH nanosheets onto $BiVO_4$.[168] The n–n heterojunction formed between CdS and $BiVO_4$ greatly enhances charge

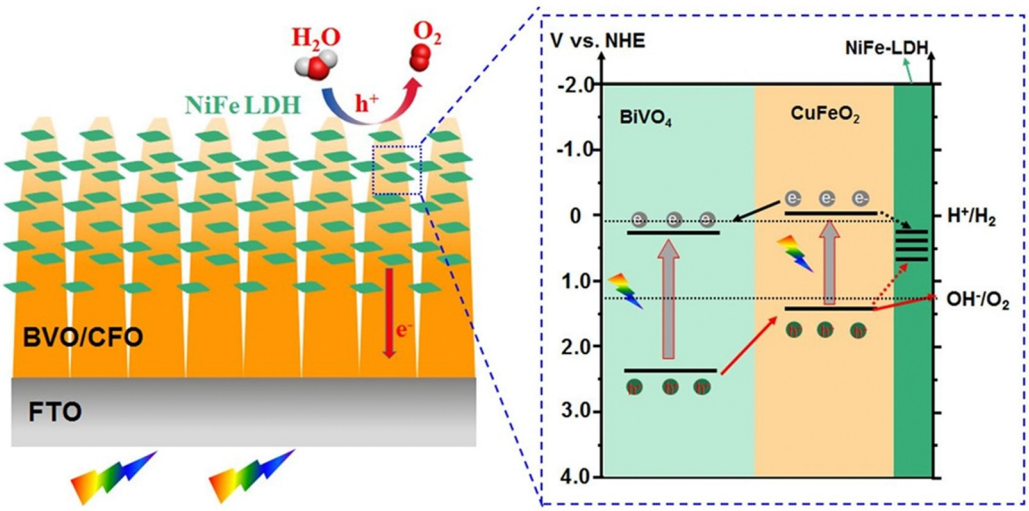

Fig. 17 The energy diagram of the $BiVO_4$/CFO/NiFe-LDH photoanode on PEC water oxidation. Reprinted with permission from ref. 171, Copyright 2022, Elsevier.

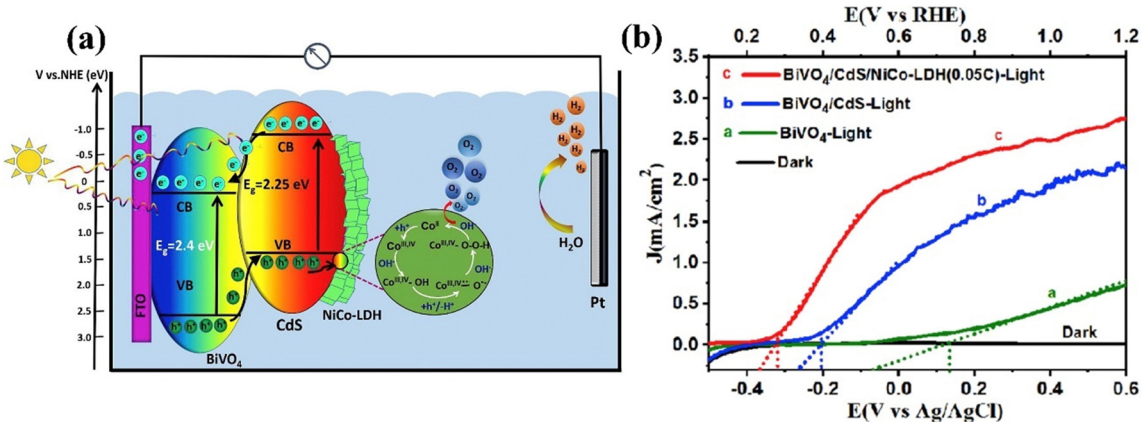

Fig. 18 (a) Schematic diagram of PEC water splitting for $BiVO_4$/CdS/NiCo-LDH. (b) Onset potentials of $BiVO_4$/MoOx/NiFe photoanode. Reprinted with permission from ref. 167, Copyright 2022, Elsevier.

separation and transfer by reducing recombination of charge carrier, while NiFe-LDH facilities faster transfer of holes from the CdS/$BiVO_4$ junction. This combined effect markedly improves the PEC properties. The $BiVO_4$/CdS/NiFe-LDH photoanode exhibited a photocurrent density of 3.1 mA cm^{-2} at 1.23 V *vs.* RHE, which is 5.8 times superior to that of the bare $BiVO_4$ photoanode and 4.9 and 4.3 times higher than those of $BiVO_4$/CdS and $BiVO_4$/NiFe-LDH photoanodes, respectively. Additionally, it exhibited a cathodic shift of 540 mV and maintains a stable photocurrent density over 3 h of irradiation.

4.3.3. Metal oxide semiconductor/$BiVO_4$/LDHs. Recently, $BiVO_4$ modified metal oxide semiconductors including α-Fe_2O_3, MoO_3, ZnO, and WO_3 have gained significant attention as photoanodes because of their stability in PEC applications, suitable band gaps, and cost-effective synthesis.[213–215] Secondary semiconductors act as electron acceptors, improving charge separation and extending the duration of charge carrier lifetimes.[216] Coupling LDHs and constructing secondary semiconductor heterojunctions are highly promising strategies for improving their PEC water splitting. For instance, Bai *et al.* developed a photoanode composed of Fe_2O_3/$BiVO_4$/NiFe-LDH.[162] In this investigation, the n–n heterojunction between Fe_2O_3 and $BiVO_4$, along with NiFe-LDH, effectively prevented the photogenerated electron–hole recombination and reduced the accumulation of holes on the photoanode surface, as shown in Fig. 19a. Consequently, the Fe_2O_3/$BiVO_4$/NiFe-LDH photoanode demonstrated a photocurrent density of 1.7 mA cm^{-2} at 1.8 V *vs.* RHE, representing a 1.3-fold increase compared to the Fe_2O_3/$BiVO_4$ photoanode.

Kolaei *et al.* developed a heterojunction photoanode consisting of WO_3/$BiVO_4$/NiFe-LDH.[163] The time-of-flight secondary ion mass spectrometry (TOF-SIMS) profile (Fig. 19b) validated the structure of the WO_3/$BiVO_4$/NiFe photoelectrode, where NiFe-LDH acts as an efficient co-catalyst. It efficiently extracts photogenerated holes from the WO_3/$BiVO_4$ photoanode surface, enabling their participation in the OER at the interface of electrode–electrolyte. Consequently, the WO_3/$BiVO_4$/NiFe photoanode was able to sustain approximately 75% of its original photocurrent over 24 h (Fig. 19c), reaching a peak photocurrent density of around 1.78 mA cm^{-2} at 1.23 V *vs.* RHE.

Singh *et al.* constructed a WO_3/$BiVO_4$-NiFeCr photoanode.[165] The study revealed that the utilization of a sputtered WO_3 underlayer in the type-II WO_3/$BiVO_4$ configuration resulted in enhanced electron–hole separation. The inclusion of Cr to NiFe-LDH enhanced its electrical conductivity. Thus, electrodeposited trimetallic NiFeCr-LDH on the WO_3/$BiVO_4$ heterojunction enhances the kinetics of water oxidation, resulting in consistent PEC water splitting performance in neutral electrolyte solution. Consequently, the WO_3/$BiVO_4$-NiFeCr photoanode achieved a photocurrent density of 4.9 mA cm^{-2} at 1.23 V *vs.* RHE,

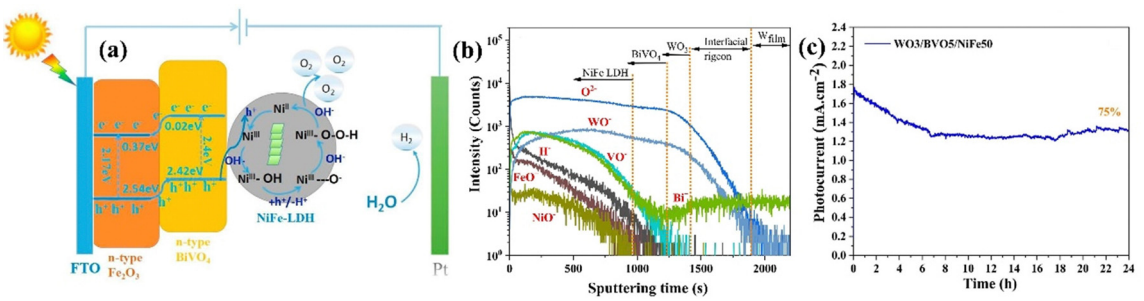

Fig. 19 (a) Schematic mechanism of PEC water splitting on Fe_2O_3/$BiVO_4$/NiFe-LDH. Reproduced with permission from ref. 162, Copyright 2018, Elsevier. (b) TOF-SIMS profile of WO_3/$BiVO_4$/NiFe-LDH, (c) Stability test of the WO_3/$BiVO_4$/NiFe-LDH photoanode. Reprinted with permission from ref. 163, Copyright 2023, Elsevier.

representing a 1.6-fold enhancement relative to $WO_3/BiVO_4$ (2.9 mA cm^{-2}) and a 1.2-fold increase compared to $WO_3/BiVO_4$-NiFe (3.8 mA cm^{-2}).

Zhou *et al.* developed a photoanode consisting of $TiO_2/BiVO_4$/NiFe-LDH.[164] The NiFe-LDH co-catalyst deposited on $TiO_2/BiVO_4$ effectively removed accumulated photogenerated holes from the surface of the photoanode. Consequently, the $TiO_2/BiVO_4$/NiFe-LDH photoanode exhibited a notable enhancement in photocurrent, achieving 17.6 μA cm^{-2}, exceeding those of the $BiVO_4$ and $TiO_2/BiVO_4$ photoanodes by factors of 3.6 and 2.5, respectively.

Bai and colleagues synthesized a new triadic photoanode consisting of $MoO_3/BiVO_4$/CoMnZn-LDH by combining metal–organic decomposition and electrodeposition techniques.[166] In this design, the $MoO_3/BiVO_4$ heterojunction effectively suppressed electron–hole recombination, whereas CoMnZn-LDH facilitated efficient hole transfer from $BiVO_4$ to the electrolyte, reducing photocorrosion and enhancing PEC water splitting efficiency. Consequently, the $MoO_3/BiVO_4$/CoMnZn-LDH photoanode demonstrated a photocurrent density of 1.24 mA cm^{-2} at 1.23 V *vs.* RHE, surpassing that of the pure $BiVO_4$ photoanode by a factor of 2.21 and 1.51-fold enhancement compared to that of $MoO_3/BiVO_4$ photoanode.

4.3.4. $BiVO_4$/electron transport layer (rGO)/LDHs. Due to the significant surface area, abundant surface defects, and rapid electron transport abilities, reduced graphene oxide (rGO) may act as a highly efficient mediator for electron transfer in the catalytic applications. The incorporation of rGO with $BiVO_4$ improves the electrical conductivity and carrier transport properties.[177,217] Integrating both rGO and LDHs into the $BiVO_4$ may greatly enhance the efficacy of PEC water splitting. For instance, Han *et al.* developed a $BiVO_4$/rGO/NiFe photoanode with an oriented hierarchical nanostructure using a simple and scalable solution method.[177] In this design, rGO serves as an intermediate layer that enhances the movement of photogenerated charge carriers, improves the adhesion of the NiFe nanoarray cocatalyst layer, and boosts both stability and PEC performance as demonstrated in Fig. 20a. As a result, the $BiVO_4$/rGO/NiFe photoelectrode reached a photocurrent density of 1.30 mA cm^{-2} at 1.23 V *vs.* RHE (Fig. 20b), which is a 3-fold increase over pure $BiVO_4$.

Sun *et al.* developed a $BiVO_4$/rGO/NiFe-LDH photoanode by sequentially loading rGO nanosheets onto $BiVO_4$ and then depositing NiFe-LDH at the $BiVO_4$/rGO interface using simple electrodeposition techniques.[178] The rGO nanosheets improve charge separation and transfer at the interface of $BiVO_4$, while NiFe-LDH acts as a cocatalyst to enhance the kinetics of water oxidation. Consequently, the photoanode achieved a photocurrent density of 1.13 mA cm^{-2} at 1.23 V *vs.* RHE, surpassing that of $BiVO_4$/rGO and pure $BiVO_4$ by factors of 1.45 and 2.17, respectively. Moreover, it showed a 124 mV cathodic shift in the onset potential when exposed to visible light.

Chen *et al.* developed a $BiVO_4$/rGO/NiFe-LDH photoanode, where NiFe-LDH serves as a catalyst for water oxidation, facilitating the transport of photo-generated holes from the $BiVO_4$ photoelectrode to the electrolyte.[180] Meanwhile, rGO nanosheets decrease electron–hole recombination by acting as an effective mediator of electron shuttling. As a result, the photocurrent density of the $BiVO_4$/rGO/NiFe-LDH photoanode increases to 3.26 mA cm^{-2} at 1.23 V *vs.* RHE, representing an increase of 2.85 times compared to bare $BiVO_4$ (1.14 mA cm^{-2}).

4.3.5. $BiVO_4$/HTL/LDHs. Introduction of a hole transport layer (HTL) into the $BiVO_4$/LDHs interface offers an efficacious approach to enhance the overall PEC water splitting performance. An appropriate HTL at the semiconductor/OEC interface can effectively enhance hole transfer and suppress the charge recombination, leading to more efficient solar water splitting on the photoanode. For instance, Wang *et al.* sequentially deposited Cu phthalocyanine (CuPc) and NiCo-LDH on a $BiVO_4$ substrate to enhance the PEC performance of the $BiVO_4$ photoanode.[173] Due to its high hole mobility, the ultrathin CuPc layer effectively retrieves photoexcited holes from $BiVO_4$ and transfers them to NiCo-LDH, which acts as the OEC to enhance the kinetics of water oxidation. Consequently, the optimized $BiVO_4$/CuPc/NiCo-LDH photoanode exhibited excellent stability and significant photocurrent density of 4.03 mA cm^{-2} at 1.23 V *vs.* RHE.

Liu *et al.* developed $BiVO_4$/FeOOH/ZnFe-LDH photoelectrodes to improve the PEC performance of $BiVO_4$.[174] In this

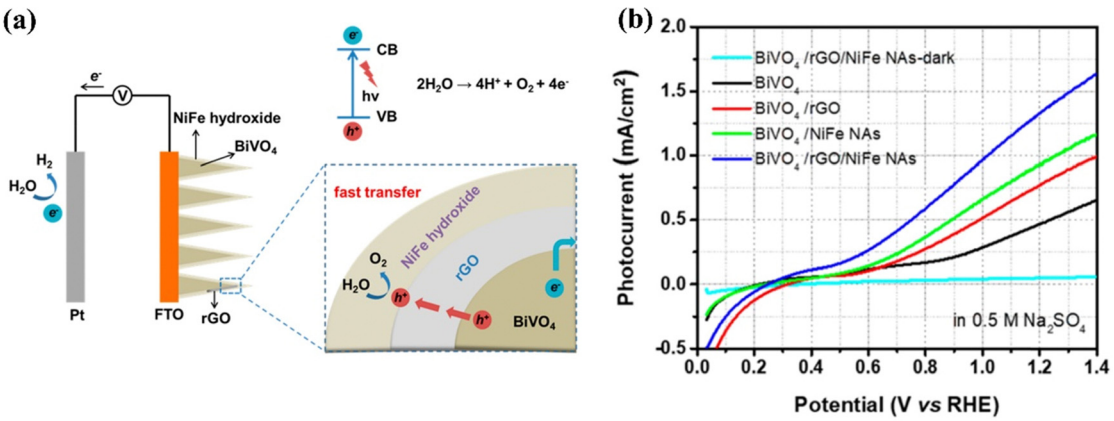

Fig. 20 (a) Schematic representation of PEC water oxidation on $BiVO_4$/rGO/NiFe (NAas) nanoarray photoanode. (b) Polarization curves of PEC response on $BiVO_4$/rGO/NiFe-LDH photoanodes. Reprinted with permission from ref.177, Copyright 2018, American Chemical Society.

design, FeOOH acts as a hole-extraction bridge between $BiVO_4$ and the ZnFe-LDH interface. The combined effects of FeOOH and ZnFe-LDH lowered the overpotential for water oxidation, enhancing the photogenerated carrier transfer and improving the kinetics of oxidation reaction. Consequently, the BVO/FeOOH/ZnFe-LDH photoelectrodes achieved a photocurrent density of 4.92 mA cm^{-2} at 1.23 V *vs.* RHE, indicating a 3.25-fold enhancement relative to bare $BiVO_4$ and a 1.4-fold increase compared to the $BiVO_4$/FeOOH electrode.

Mohanta *et al.* used a thin layer of two-dimensional boron nitride nanoplatelets (BNNPs) as an ultra-rapid hole extractor and developed a $BiVO_4$/BNNPs/CoCr-LDH photoanode for PEC water splitting,[175] where CoCr-LDH enhances reaction kinetics (Fig. 21a). Therefore, the $BiVO_4$/BNNPs/CoCr-LDH photoanode showed a cathodic shift of about 360 mV and a photocurrent density of 3.8 mA cm^{-2} at 1.23 V *vs.* RHE (Fig. 21b), 3.2-fold greater than that of bare $BiVO_4$.

Alam *et al.* employed graphene quantum dots (GQDs) as conductive linkers to extract holes from the $BiVO_4$ surface and developed a $BiVO_4$/GQDs/CoSn-LDH photoanode, where CoSn-LDH provides surface-active centers.[179] As a result, the photocurrent density of the $BiVO_4$/GQDs/CoSn-LDH photoanode attains 4.15 mA cm^{-2}, which is threefold greater than that of bare $BiVO_4$, due to the synergistic impact of GQDs and CoSn-LDH in facilitating hole extraction and transport to the surface reaction site. Furthermore, the photoanode exhibited improved stability, maintaining 90% of its initial performance following 4 h of continuous exposure to light.

4.3.6. Others. Localized surface plasmon resonance (LSPR) in materials enhances the electromagnetic field near the plasmonic nanomaterials such as Au and Ag, accelerating charge separation in neighboring catalysts. These plasmonic effects can also be utilized to boost PEC water splitting.[218–220] Wang *et al.* employed the LSPR effect of Au to develop a three-layer photoanode with plasmonic Au–SiO_2 nanoparticles, CoAl-LDHs, and $BiVO_4$, and designed two configurations: CoAl-LDH/Au@SiO_2/$BiVO_4$ (photoanode-I) and Au@SiO_2/CoAl-LDH/$BiVO_4$ (photoanode-II).[181] In these designs, Au–SiO_2 nanoparticles generated LSPR, and CoAl-LDH facilitated water oxidation. The strong LSPR generated by Au@SiO_2 in photoanode-I promotes charge separation in $BiVO_4$, leading to a photocurrent density of 1.92 mA cm^{-2}, 52% higher than that of photoanode-II (Fig. 22(a–f)).

Recently, Bai *et al.* designed an OH-$BiVO_4$@C/NiFe-LDH composite photoanode for PEC water splitting.[182] The study found that the addition of a carbon layer improved electronic conductivity and significantly polarized the electronic field due to hydroxylation, facilitating both interfacial charge transfer and bulk charge separation. Consequently, the optimized photoanode achieved an impressive photocurrent density of 5.31 mA cm^{-2} at 1.23 V *vs.* RHE. Furthermore, the stability of the OH-$BiVO_4$@C@NiFe-LDH photoanode was significantly enhanced by the protective carbon layer and the improved redeposition of Fe active sites in NiFe-LDH catalysts, which was induced by increased adsorption of Fe(III) onto Ni sites *via* hydroxylation. After 20 h of irradiation, the material maintained over 87.5% of its initial photocurrent density, owing to a self-healing mechanism (Fig. 23).

4.4. $BiVO_4$/LDH composites

Exfoliating the lamellar structure of LDHs or coupling them with carbon-based materials, QDs, and single atom catalysts is critical for the OER due to the ability of LDH composites to generate numerous catalytic active sites, enhance electrical conductivity, and facilitate the movement of electrolyte ions. Therefore, constructing LDH composites with $BiVO_4$ is an exceptionally efficient technique for enhancing the PEC performance of bare $BiVO_4$. For example, graphene is known as a 2D layered carbon material, exhibiting exceptional electrical conductivity and metal-like properties. Utilizing the advantages of graphene, Zhang *et al.* developed the $BiVO_4$@CoAl-LDH@graphen triadic photoanode through a one-step hydrothermal method.[75] In this design, CoAl-LDH expedites the kinetics of water oxidation, whereas graphene promotes the transfer of photo-generated charges, thus extending the distance of carrier transfer within the charge transfer channels, efficiently inhibiting carrier recombination, and enhancing water oxidation efficiency, as depicted in Fig. 24a. Consequently, $BiVO_4$@-CoAl-LDH@graphen photoanode demonstrated a photocurrent density of 2.13 mA cm^{-2} at 1.23 V *vs.* RHE, which is fourfold

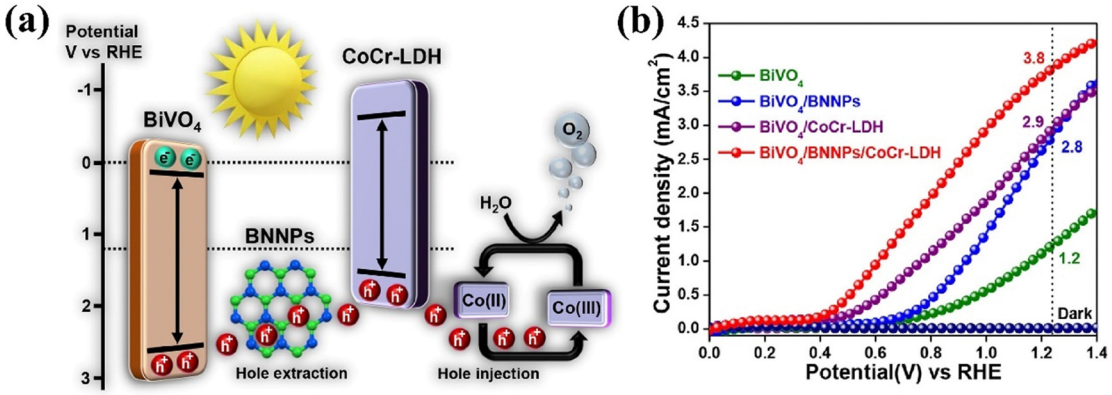

Fig. 21 (a) PEC mechanism of the $BiVO_4$/BNNPs/CoCr-LDHs photoanode (b) LSV of the $BiVO_4$/BNNPs/CoCr-LDH photoanode under 1 sun illumination. Reproduced with permission from ref. 175, Copyright 2022, Elsevier.

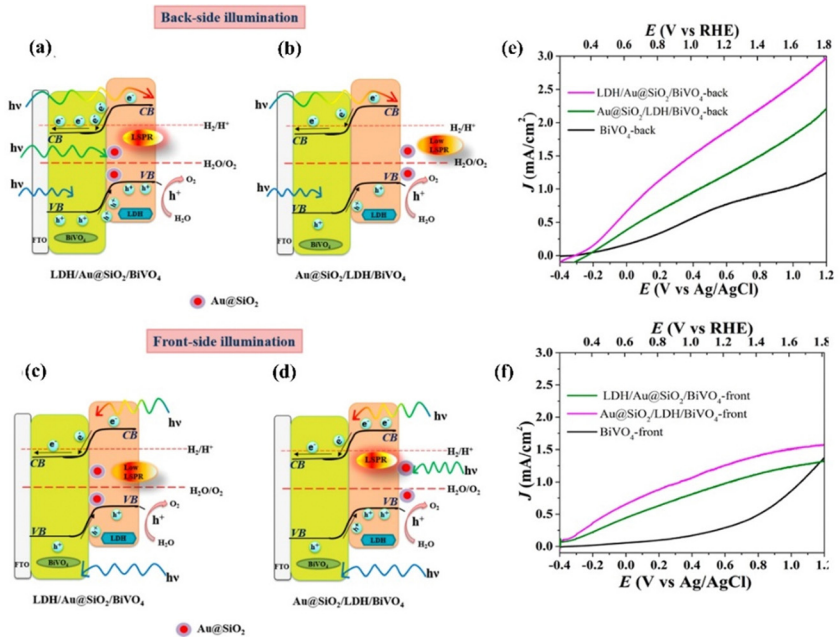

Fig. 22 Energy levels and photogenerated charge-transfer process in composite photoanodes of $BiVO_4/SiO_2$@Au/LDH(Left) and $BiVO_4$/LDH/SiO_2@Au (Right) under irradiation from (a) and (b) back-side and (c) and (d) front-side. The respective LSV curves for (e) back-side and (f) front-side illumination. Reprinted with permission from ref. 181, Copyright 2018, American Chemical Society.

greater than that of pure $BiVO_4$. Moreover, the oxidation efficiency remained impressive at 80% under low voltage (Fig. 24b). Additionally, IPCE of $BiVO_4$@CoAl-LDH@graphen was 52% at 400 nm.

The inclusion of CDs into NiFe-LDH enhances its electrical conductivity and electrocatalytic activity, leading to improved overall PEC performance in water splitting. By sequentially incorporating NiFe-LDH and CDs onto the $BiVO_4$ photoanode, Lv *et al.* developed a ternary $BiVO_4$/NiFe-LDH/CDs photoanode for PEC water splitting.[184] In this design, NiFe-LDH effectively enhances the kinetics of oxygen evolution. Additionally, the incorporation of CDs reduces overpotential and charge transfer resistance during the oxygen evolution process. Consequently, the resulting ternary $BiVO_4$/NiFe-LDH/CDs photoanode exhibited a notable increase in photocurrent, reaching 2.84 mA cm^{-2} at 1.23 V *vs.* RHE.

CdTe QDs possess outstanding light-harvesting and charge-transfer properties, thus can be used as charge transfer promoters or photo sensitizers in PEC photoelectrodes. Tang *et al.* created a triadic $BiVO_4$@CoAl-LDH@CdTeQD photoanode by sequentially depositing red- and green-emission CdTe QDs from an aqueous solution onto the CoAl-LDH/$BiVO_4$ photoanode, as shown in Fig. 25a.[185] The successive Type-II band alignments of CdTeQD@CoAl-LDH and $BiVO_4$@CoAl-LDH enhance movements of electron to the counter electrode and facilitate hole migration to the surface throughout water oxidation. Moreover, the isolated anchoring and uniform distribution of CdTe QDs on 2D CoAl-LDH nanosheets improve light harvesting, charge separation, and

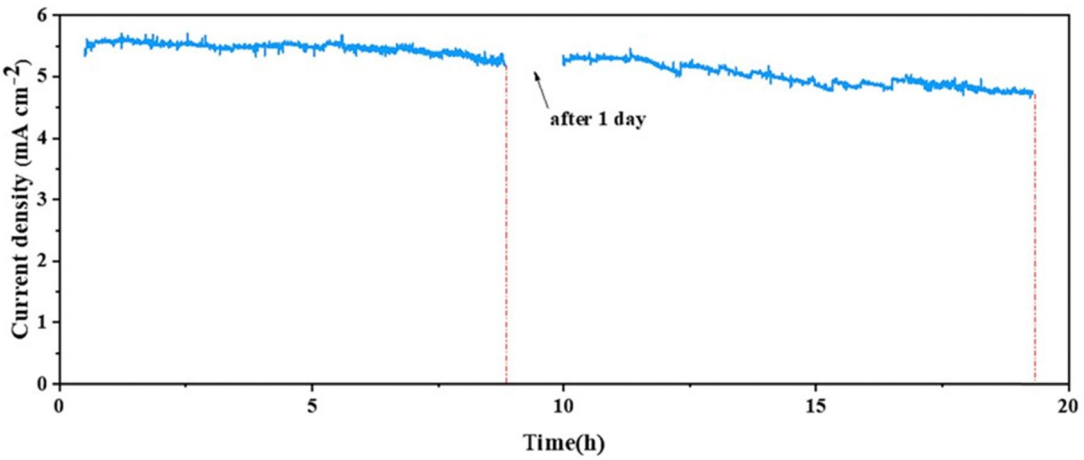

Fig. 23 Long-term stability test for the OH-$BiVO_4$@C@NiFe-LDH photoanode [KBi + 100 μM Fe(III)], ref.182, Copyright 2024, Elsevier.

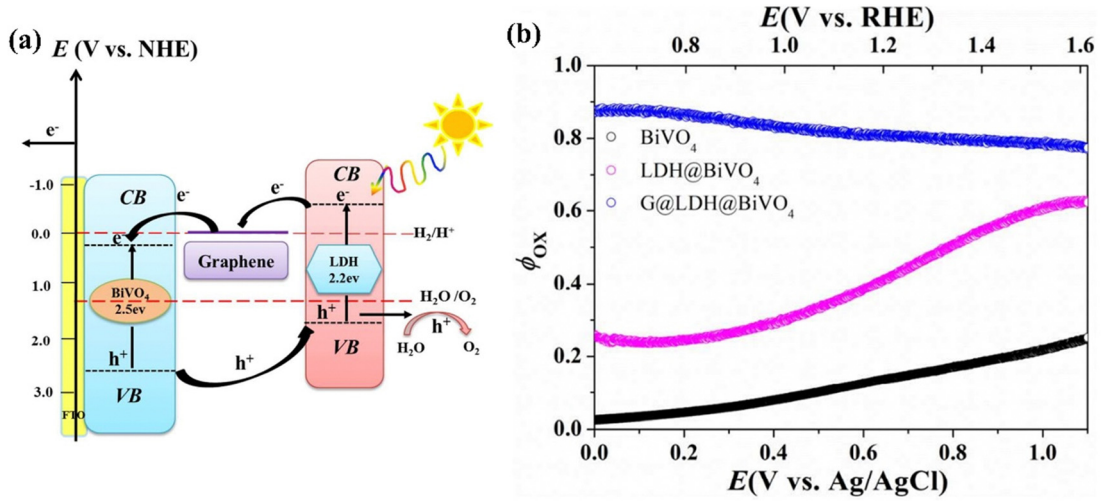

Fig. 24 (a) Charge transfer mechanism and (b) oxidation efficiency (Φ_{ox}) of $BiVO_4$@LDH graphene photoanodes. Reprinted with permission from ref. 75, Copyright 2017, American Chemical Society.

hole extraction, potentially *via* the transfer of hot electrons or holes (Fig. 25b). Therefore, the $BiVO_4$@CoAl-LDH@CdTeQD photoanode exhibited a photocurrent density of 2.23 mA cm^{-2} at 1.23 V *vs.* RHE, which is twice as compared to that of dyadic $BiVO_4$@CoAl-LDH. Furthermore, the efficiency of water oxidation surpasses 90% at a low potential of 0.5 V *vs.* RHE (Fig. 25c).

Moreover, LDHs can be easily exfoliated into monolayers through chemical or mechanical exfoliation techniques. The obtained ultrathin layers exhibit a substantial number of exposed active sites and a vast surface area, leading to high intrinsic catalytic activity.[89,221] Loading ultrathin nanosheet LDHs onto $BiVO_4$ photoanodes is an effective approach to improve the overall PEC performance of $BiVO_4$. For example, Zhong *et al.* fabricated a Mo:$BiVO_4$/CoAl-LDH photoanode for PEC water splitting.[132] The authors studied two different LDHs, bulk (b) CoAl-LDH and ultrathin (u)-CoAl-LDH, on Mo:$BiVO_4$ using a dip coating method. Among these, the u-CoAl-LDH on Mo:$BiVO_4$ demonstrated superior photoexcited charge separation, as confirmed by LSV measurements and open-circuit potential investigation. As shown in Fig. 26a, under illumination, the current density of Mo: $BiVO_4$/u-CoAl-LDH achieves 5.8 mA cm^{-2} at 1.23 V *vs.* RHE, representing an increase of 1.5 and 3.62 times compared to Mo:$BiVO_4$ and $BiVO_4$, respectively. This suggests that the ultrathin structure enhances the photogenerated charge carrier movement because of its shorter charge transport path, whereas the bulk one impedes hole transit. Furthermore, compared to Mo:$BiVO_4$, the Mo:$BiVO_4$/u-CoAl-LDH photoanode demonstrates a notably higher photovoltage of 0.38 V, suggesting an improved driving force for effective charge separation (Fig. 26b). Additionally, the Mo:$BiVO_4$/u-CoAl-LDH photoanode demonstrated self-healing capabilities due to the facile repair of oxygen defects in u-CoAl-LDH *via* the Co^{3+}/Co^{2+} cycle, allowing the PEC performance to naturally restore in the air (Fig. 26c).

Feng *et al.* synthesized hollow dodecahedral NiCo-LDH (HD-NiCo-LDH) and lamellar NiCo-LDH (NiCo-LDH), which were loaded onto the $BiVO_4$ photoanode for PEC water splitting.[188] As illustrated in Fig. 26(d and e), the stacking of ultra-thin nanosheets in HD-NiCo-LDH produces a higher specific surface area and pore size compared to NiCo-LDH. This leads to an abundance of active catalytic sites and promotes the effective extraction and separation of photogenerated holes. Consequently, the $BiVO_4$/HD-NiCo-LDH photoanode exhibited a photocurrent density of 4.54 mA cm^{-2} at 1.23 V *vs.* RHE (Fig. 26f), representing increases of 1.39 and 3.46 times compared to the $BiVO_4$/NiCo-LDH and bare $BiVO_4$ photoanodes, respectively.

Coupling single atom noble metals such as Pt or Ru to LDHs may result in electronic interaction between the LDHs' support and single atoms, resulting in increased catalytic activity, selectivity and stability of the catalyst. Incorporating NiFe-LDH-supported single Ru atoms on to $BiVO_4$, Sun *et al.* developed a $BiVO_4$@NiFe-LDHs/Ru photoanode for PEC water splitting.[186] The Cs coated STEM (Fig. 27a and b) and EXAFS (Fig. 27c) provided strong evidence that the Ru atoms are anchored to NiFe-LDHs through oxygen coordination, resulting in the formation of Ru–O–M bonds. These bonds facilitate electron rearrangement, leading to enhanced charge carrier separation and injection. Consequently, $BiVO_4$@NiFe-LDHs/Ru achieved a high photocurrent density of 4.65 mA cm^{-2} at 1.23 V *vs.* RHE. Moreover, the XPS spectra showed that the presence of Ru atoms causes the $V^{(5-x)+}$ ions to form, which helps stabilize the V atoms in the lattice of $BiVO_4$ and prevents V^{5+} dissolution during the process of PEC water oxidation. It maintained 94.8% of its original photocurrent density value over a period of 5 h. The DFT calculations indicated that Ru single atoms anchored to $BiVO_4$@NiFe-LDHs decrease the reaction energy barrier of the rate-limiting step (*O → *OOH), thus facilitating the OER process (Fig. 27d).

Gao *et al.* developed a $BiVO_4$/AC-CoFe/Pt photoanode by incorporating an amorphous/crystalline (A/C) CoFe LDH heterostructure with a single atomic Pt supported on $BiVO_4$ photoanodes.[187] In this design, the single atom (SA) Pt/AC-CoFe catalyst exhibited a much lower overpotential of 230 mV

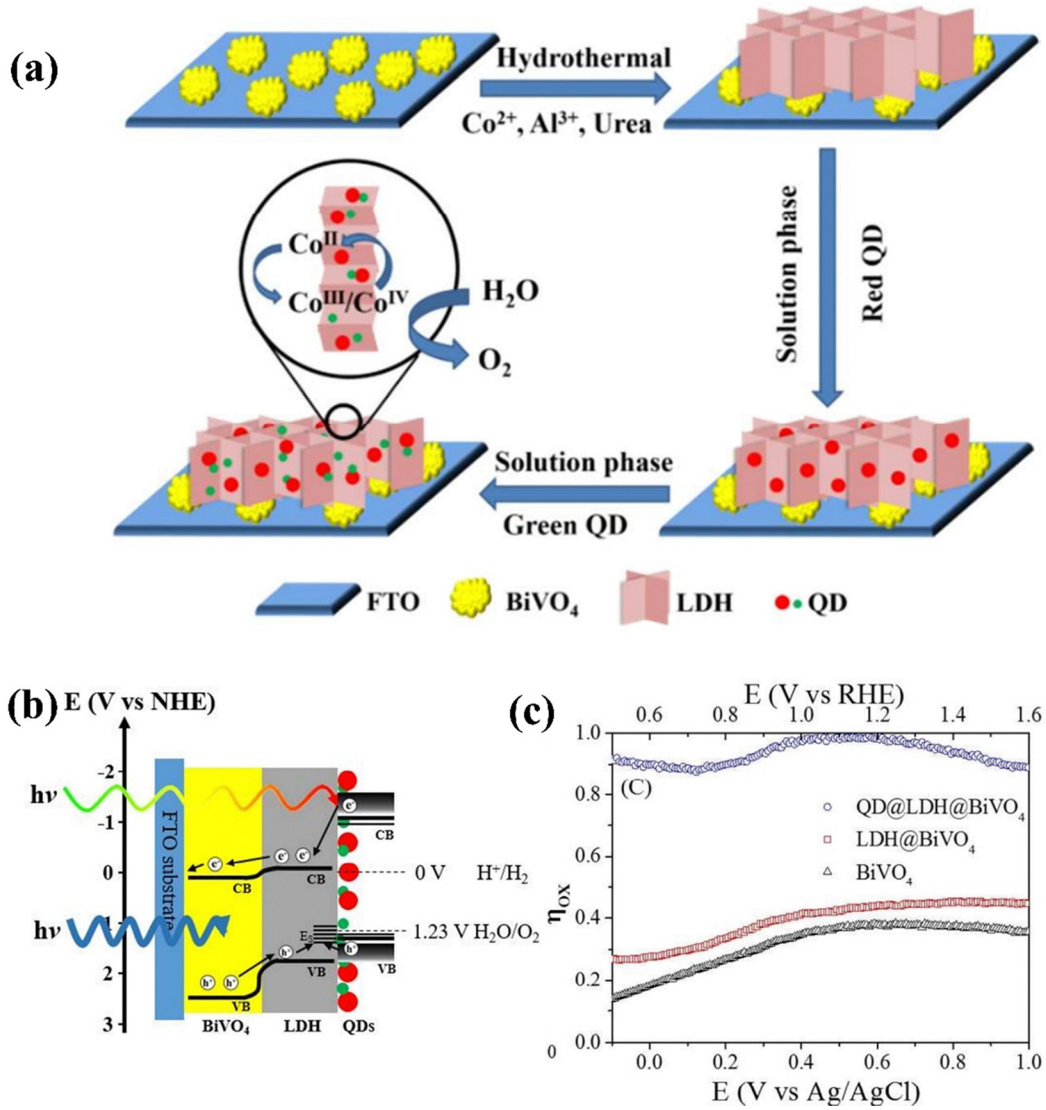

Fig. 25 (a) Synthesis process, (b) charge transfer pathways, and (c) oxidation efficiency (Φ_{ox}) of $BiVO_4$@LDH@QD photoanodes. Reprinted with permission from ref. 185, Copyright 2016, American Chemical Society.

at 10 mA cm^{-2} compared to the AC-CoFe catalyst, as shown in Fig. 28a. In addition to enhancing the OER process, the SAs Pt anchored on the AC-CoFe catalyst also improves charge separation and transport within the $BiVO_4$ photoelectrode. The SAs Pt/AC-CoFe/$BiVO_4$ exhibited an outstanding photocurrent density of 5.14 mA cm^{-2} at 1.23 V *vs.* RHE (Fig. 28b), which is 3.0 and 1.6 times greater than that of bare $BiVO_4$ and AC-CoFe/$BiVO_4$, respectively, and it also demonstrated a stability for 20 h (Fig. 28c).

5. Conclusion and outlook

$BiVO_4$ is a prominent visible light semiconductor photoanode for PEC water splitting. Combining LDHs with $BiVO_4$ photoanodes provides a significant breakthrough in PEC water splitting due to their synergistic properties. LDHs improve charge separation and decrease recombination, addressing key limitations of $BiVO_4$, including sluggish reaction kinetics and inadequate charge transport. This integration lowers the reaction overpotential and boosts the OER kinetics, leading to enhanced overall performance of the PEC system. This review explored various composite structures, including $BiVO_4$ combined with bimetallic and trimetallic LDHs, as well as other $BiVO_4$-based composites like $BiVO_4$/metal oxides, metal sulfides, and various charge transport layers integrated with LDHs. It also covered LDH composites incorporating materials such as graphene, CDs, QDs, and single-atom catalysts, along with techniques for surface engineering and LDH exfoliation with $BiVO_4$. The main intention of the integration of LDHs with $BiVO_4$ demonstrated significant improvements in photocurrent density, onset potential, and overall stability, making these composites attractive for sustainable hydrogen production. However, despite these advancements, challenges

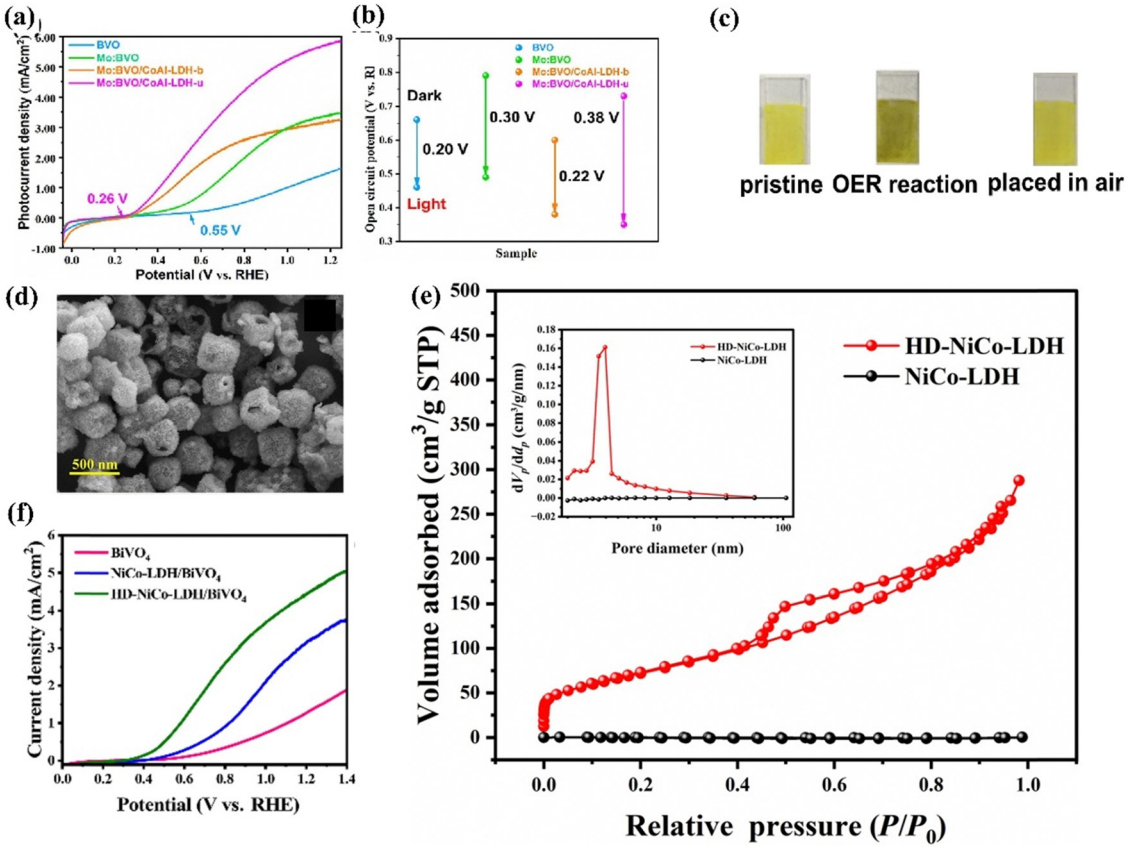

Fig. 26 (a) Photocurrent, (b) open circuit potential, and (c) photographs of Mo:$BiVO_4$/u-CoAL-LDH photoanode films before and after reaction, and being placed in the air for one day. Reprinted with permission from ref. 132, Copyright 2023, Elsevier. (d) SEM image, (e) N_2 adsorption isotherm and pore size distribution curves, and (f) LSV curves of $BiVO_4$/HD-NiCo-LDH photoanodes. Reprinted from ref. 188, CC. BY 4.0.

remain in optimizing the interface, improving stability, and enhancing overall efficiency. In accordance with the discussions in this review, the following obstacles and prospects are identified as critical to the advancement of the development of high-performance $BiVO_4$/LDH composites for PEC water splitting.

(i) Despite significant progress in coupling transition metal based LDHs with $BiVO_4$ photoanodes for PEC water splitting, challenges concerning stability and efficiency still hinder their widespread implementation in practical applications. The interfacial charge recombination between LDHs and $BiVO_4$ is a significant obstacle that affects the charge transfer efficiency. To address this issue, future research ought to focus on interface engineering to further improve charge separation and reduce recombination. By employing various methods like interlayers such as hole storage, electron transport layer, and doping, advanced heterojunctions, it is possible to effectively eliminate the interfacial energy barriers. This facilitates the rapid transfer of holes through the chemical bonding of LDHs and $BiVO_4$, ultimately resulting in enhanced effectiveness of the PEC process. Moreover, Since LDHs remain stable in alkaline electrolytes, future studies should focus on ensuring their stability under harsh solution conditions and solar irradiation. Developing self-healing materials, protective coatings, and degradation prevention strategies will be critical for ensuring the long-term functioning of $BiVO_4$/LDH photoanodes. Furthermore, due to the low conductivity and limited specific surface area of traditional LDHs, research into new LDH compositions such as multi-metal LDHs, QD-incorporated LDHs, and single-atom catalysts could lead to the discovery of materials with superior catalytic properties, specifically tailored for improved performance in $BiVO_4$/LDH composites.

(ii) Due to their tunable compositional and structural features, LDHs serve as a versatile catalytic structure capable of addressing kinetically challenging reactions. Optimizing the loading conditions of LDHs onto $BiVO_4$ photoanodes is critical for improving PEC efficiency. Excessive loading can potentially hinder the efficient light absorption by $BiVO_4$, whereas inadequate loading may result in a lack of sufficient catalytic sites. To achieve the desired balance, it is necessary to have precise control over the deposition process as well as a thorough understanding of the interaction between LDHs and $BiVO_4$. Advanced characterization techniques could play an important role in optimizing the loading process to achieve outstanding performance. Moreover, the role of specific intercalated anions within LDHs on the PEC water splitting performance of $BiVO_4$/LDHs composites remains yet to be explored, offering a promising direction for future research.

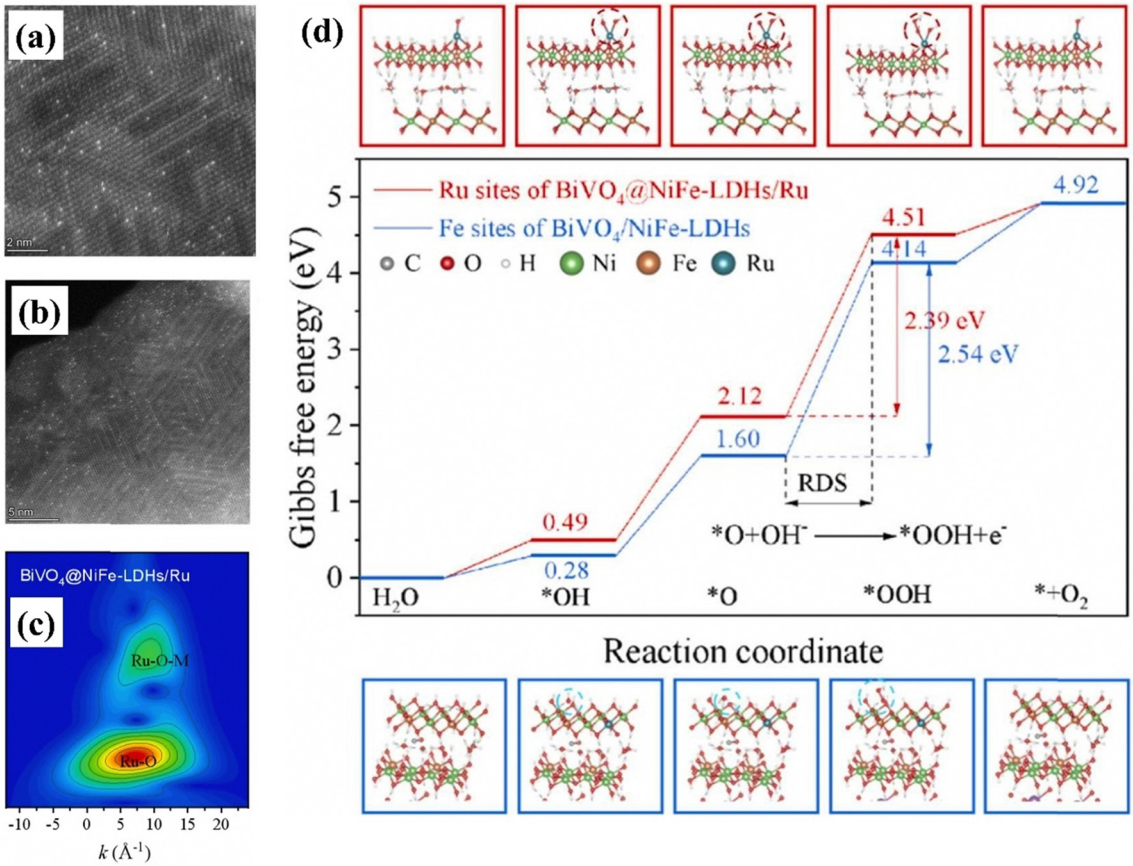

Fig. 27 (a) and (b) Cs-corrected STEM images, (c) WT-EXAFS signals of the $BiVO_4$@NiFe-LDH/Ru photoanode. (d) Free energy diagram of the OER process for $BiVO_4$@NiFe-LDHs and $BiVO_4$@NiFe-LDHs/Ru photoanodes. Reprinted with permission from ref. 186, Copyright 2023, Elsevier.

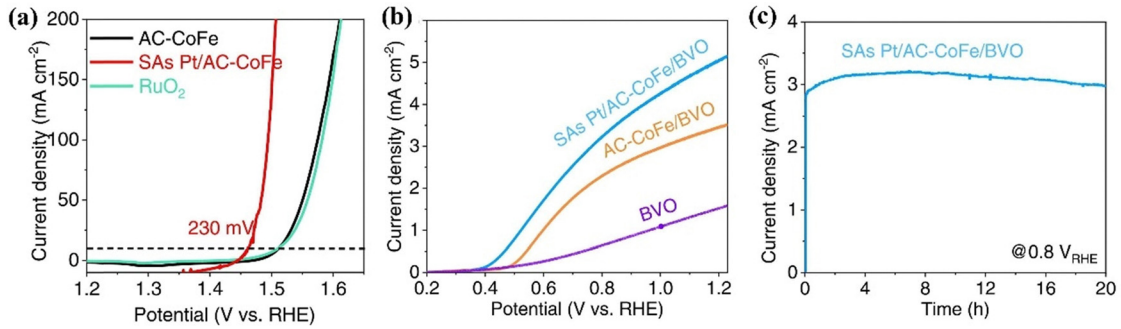

Fig. 28 (a) LSV curves of RuO_2, AC-CoFe, and SAs pt/AC-CoFe in 1 M KOH and (b) $BiVO_4$/AC-CoFe/SAsPt photoanodes under AM 1.5G illumination. (c) Stability of the $BiVO_4$/AC-CoFe/SAsPt photoanode in 1 M KBi. Reprinted with permission from ref. 187, Copyright 2023, Elsevier.

(iii) Understanding the intrinsic mechanism of PEC water oxidation is critical for selection and modification of photoanodes. In addition to the extensive studies on morphology, elemental composition, and valence states, the advancement of *in situ* characterization techniques like X-ray absorption spectroscopy (XAS), transient absorption spectroscopy (TAS), and operando spectroscopic studies is crucial for understanding surface charge transfer, identifying active sites, and elucidating reaction kinetics in the PEC water splitting process.[38,222,223] Moreover, direct visualization of electron transfer between atoms is made possible by *in situ* irradiation X-ray photoelectron spectroscopy (SIXPS), thereby rendering it easier to investigate the movement and separation of charges during atom activation.[224] Furthermore, computational techniques, such as density functional theory (DFT), and machine learning approaches hold significant potential for predicting and selecting materials, identifying adsorption sites, and extrapolating reaction pathways.[225–227] Therefore, the integration of experimental techniques with

theoretical calculations is essential for unraveling the intricate mechanisms in LDH modified $BiVO_4$ systems.

(iv) Since theoretical efficiency of the $BiVO_4$ photoanode is close to 9.1%, it stands as a potentially effective material for achieving high PEC water splitting efficiency through unbiased photoanode-PV and photoanode-photocathode configurations.[228,229] The $BiVO_4$-photocathode tandem is regarded as more desirable for practical applications due to its lower cost and simpler electrical connection compared to the $BiVO_4$-PV configuration.[230,231] Therefore, developing efficient photocathodes is another big challenge to improve the STH efficiency of $BiVO_4$ photoanodes in unbiased PEC water splitting systems. The coupling of $BiVO_4$ with improved photocathodes and LDHs holds great promise for boosting STH efficiency, advancing PEC water splitting technology toward practical applications. We expect that the utilization of $BiVO_4$ photoanodes and LDHs will lead to significant progress in the coming years.

Data availability

No primary research results, software or code have been included and no new data were generated or analysed as part of this review.

Conflicts of interest

There are no conflicts to declare.

Acknowledgements

This work was supported by the Japan Society for the Promotion of Science (JSPS KAKENHI) Grant Number JP23K26377.

References

1 J. Deng, Y. Su, D. Liu, P. Yang, B. Liu and C. Liu, *Chem. Rev.*, 2019, **119**, 9221–9259.
2 J. Barber, *Chem. Soc. Rev.*, 2009, **38**, 185–196.
3 M. M. Abouelela, G. Kawamura, W. K. Tan and A. Matsuda, *J. Colloid Interface Sci.*, 2023, **629**, 958–970.
4 C. Liu, N. P. Dasgupta and P. Yang, *Chem. Mater.*, 2014, **26**, 415–422.
5 F. Yilmaz, M. T. Balta and R. Selbaş, *Renewable Sustainable Energy Rev.*, 2016, **56**, 171–178.
6 U. Asghar, S. Rafiq, A. Anwar, T. Iqbal, A. Ahmed, F. Jamil, M. S. Khurram, M. M. Akbar, A. Farooq, N. S. Shah and Y.-K. Park, *J. Environ. Chem. Eng.*, 2021, **9**, 106064.
7 M. Ali, E. Pervaiz, T. Noor, O. Rabi, R. Zahra and M. Yang, *Int. J. Energy Res.*, 2021, **45**, 1190–1226.
8 P. A. Koyale and S. D. Delekar, *Int. J. Hydrogen Energy*, 2024, **51**, 515–530.
9 C. V. Reddy, K. R. Reddy, N. P. Shetti, J. Shim, T. M. Aminabhavi and D. D. Dionysiou, *Int. J. Hydrogen Energy*, 2020, **45**, 18331–18347.
10 M. A. Gaikwad, U. P. Suryawanshi, U. V. Ghorpade, J. S. Jang, M. P. Suryawanshi and J. H. Kim, *Small*, 2022, **18**, 2105084.
11 C. Jiang, S. J. A. Moniz, A. Wang, T. Zhang and J. Tang, *Chem. Soc. Rev.*, 2017, **46**, 4645–4660.
12 S. Wang, X. Wang, B. Liu, Z. Guo, K. (Ken) Ostrikov, L. Wang and W. Huang, *Nanoscale*, 2021, **13**, 17989–18009.
13 Y. Qiu, Z. Pan, H. Chen, D. Ye, L. Guo, Z. Fan and S. Yang, *Sci. Bull.*, 2019, **64**, 1348–1380.
14 K. Wang, D. Huang, X. Li, K. Feng, M. Shao, J. Yi, W. He and L. Qiao, *Electron*, 2023, **1**, e4.
15 A. Raveendran, M. Chandran and R. Dhanusuraman, *RSC Adv.*, 2023, **13**, 3843–3876.
16 I. R. Hamdani and A. N. Bhaskarwar, *Renewable Sustainable Energy Rev.*, 2021, **138**, 10503.
17 L. Fu, Z. Li and X. Shang, *Int. J. Hydrogen Energy*, 2024, **55**, 611–624.
18 S. Chen, T. Takata and K. Domen, *Nat. Rev. Mater.*, 2017, **2**, 17050.
19 C. Li, W. Fan, S. Chen and F. Zhang, *Chem. – Eur. J.*, 2022, **28**, e202201812.
20 L. Wang, Y. Zhang, W. Li and L. Wang, *Mater. Rep.: Energy*, 2023, **3**, 100232.
21 W. Wang, M. Xu, X. Xu, W. Zhou and Z. Shao, *Angew. Chem., Int. Ed.*, 2020, **59**, 136–152.
22 A. Vilanova, P. Dias, T. Lopes and A. Mendes, *Chem. Soc. Rev.*, 2024, **53**, 2388–2434.
23 M. M. Abouelela, G. Kawamura and A. Matsuda, *J. Cleaner Prod.*, 2021, **294**, 126200.
24 P. P. Edwards, V. L. Kuznetsov, W. I. F. David and N. P. Brandon, *Energy Policy*, 2008, **36**, 4356–4362.
25 B. S. Kalanoor, H. Seo and S. S. Kalanur, *Mater. Sci. Energy Technol.*, 2018, **1**, 49–62.
26 M. Lee, S. Haas, V. Smirnov, T. Merdzhanova and U. Rau, *ChemElectroChem*, 2022, **9**, e202200838.
27 L. Ding, Y. Zhang, T. Wang, P. Li and K. Chang, *Catal. Sci. Technol.*, 2024, **14**, 1730–1755.
28 J. H. Kim, D. Hansora, P. Sharma, J.-W. Jang and J. S. Lee, *Chem. Soc. Rev.*, 2019, **48**, 1908–1971.
29 S. Li, W. Xu, L. Meng, W. Tian and L. Li, *Small Sci.*, 2022, **2**, 2100112.
30 L. Clarizia, M. N. Nadagouda and D. D. Dionysiou, *Curr. Opin. Green Sustainable Chem.*, 2023, **41**, 100825.
31 S. Tembhurne, F. Nandjou and S. Haussener, *Nat. Energy*, 2019, **4**, 399–407.
32 R. Lin, H. Lei, D. Ruan, K. Jiang, X. Yu, Z. Wang, W. Mai and H. Yan, *Nano Energy*, 2019, **56**, 82–91.
33 M. Joseph, M. Kumar, S. Haridas, C. Subrahmanyam and S. N. Remello, *Energy Adv.*, 2024, **3**, 30–59.
34 M. Mohamed Abouelela, G. Kawamura and A. Matsuda, *J. Energy Chem.*, 2022, **73**, 189–213.
35 A. Fujishima and K. Honda, *Nature*, 1972, **238**, 37–38.
36 A. G. Tamirat, J. Rick, A. A. Dubale, W.-N. Su and B.-J. Hwang, *Nanoscale Horiz.*, 2016, **1**, 243–267.
37 Y. Wang, W. Tian, C. Chen, W. Xu and L. Li, *Adv. Funct. Mater.*, 2019, **29**, 1809036.

38 G. Dong, L. Yan and Y. Bi, *J. Mater. Chem. A*, 2023, **11**, 3888–3903.
39 H. Sun, J. Dai, W. Zhou and Z. Shao, *Energy Fuel*, 2020, **34**, 10547–10567.
40 P. Mane, I. V. Bagal, H. Bae, A. N. Kadam, V. Burungale, J. Heo, S.-W. Ryu and J.-S. Ha, *Int. J. Hydrogen Energy*, 2022, **47**, 39796–39828.
41 D. Cui, L. Wang, K. Xu, L. Ren, L. Wang, Y. Yu, Y. Du and W. Hao, *J. Mater. Chem. A*, 2018, **6**, 2193–2199.
42 R. Siavash Moakhar, S. M. Hosseini-Hosseinabad, S. Masudy-Panah, A. Seza, M. Jalali, H. Fallah-Arani, F. Dabir, S. Gholipour, Y. Abdi, M. Bagheri-Hariri, N. Riahi-Noori, Y. Lim, A. Hagfeldt and M. Saliba, *Adv. Mater.*, 2021, **33**, 2007285.
43 W. Jiang, C. Ni, L. Zhang, M. Shi, J. Qu, H. Zhou, C. Zhang, R. Chen, X. Wang, C. Li and R. Li, *Angew. Chem.*, 2022, **134**, e202207161.
44 R. L. Spray and K.-S. Choi, *Chem. Mater.*, 2009, **21**, 3701–3709.
45 G. Wang, Y. Ling, H. Wang, X. Yang, C. Wang, J. Z. Zhang and Y. Li, *Energy Environ. Sci.*, 2012, **5**, 6180.
46 A. U. Pawar, C. W. Kim, M. J. Kang and Y. S. Kang, *Nano Energy*, 2016, **20**, 156–167.
47 I. Chauhan, K. K. Patra, H. Bajpai, N. B. Mhamane, K. N. Salgaonkar and C. S. Gopinath, *Dalton Trans.*, 2023, **52**, 2051–2061.
48 M. Zhong, J. Shi, F. Xiong, W. Zhang and C. Li, *Sol. Energy*, 2012, **86**, 756–763.
49 A. D. DeAngelis, K. C. Kemp, N. Gaillard and K. S. Kim, *ACS Appl. Mater. Interfaces*, 2016, **8**, 8445–8451.
50 B. R. Lee, S. Choi, W. S. Cheon, J. W. Yang, M. G. Lee, S. H. Park and H. W. Jang, *Electron. Mater. Lett.*, 2022, **18**, 391–399.
51 G. Lv, L. Long, X. Wu, Y. Qian, G. Zhou, F. Pan, Z. Li and D. Wang, *Appl. Surf. Sci.*, 2023, **609**, 155335.
52 J. Fu, Z. Fan, M. Nakabayashi, H. Ju, N. Pastukhova, Y. Xiao, C. Feng, N. Shibata, K. Domen and Y. Li, *Nat. Commun.*, 2022, **13**, 729.
53 X. Shen, T. Zhao, H. Su, M. Yang, J. Chen, Y. Liu, R. Yanagi, D. Solanki and S. Hu, *Adv. Energy Mater.*, 2022, **12**, 2201314.
54 H. Huang, L. Liu, Y. Zhang and N. Tian, *RSC Adv.*, 2015, **5**, 1161–1167.
55 S. Mary, C. Murugan and A. Pandikumar, *J. Colloid Interface Sci.*, 2022, **608**, 2482–2492.
56 M. N. Shaddad, P. Arunachalam, M. Hezam, N. M. BinSaeedan, S. Gimenez, J. Bisquert and A. M. Al-Mayouf, *J. Catal.*, 2023, **418**, 51–63.
57 A. Kudo, K. Omori and H. Kato, *J. Am. Chem. Soc.*, 1999, **121**, 11459–11467.
58 P. Subramanyam, T. Khan, G. Neeraja Sinha, D. Suryakala and C. Subrahmanyam, *Int. J. Hydrogen Energy*, 2020, **45**, 7779–7787.
59 S. Alam, T. K. Sahu and M. Qureshi, *ACS Sustainable Chem. Eng.*, 2021, **9**, 5155–5165.
60 Y. Qiu, W. Liu, W. Chen, W. Chen, G. Zhou, P.-C. Hsu, R. Zhang, Z. Liang, S. Fan, Y. Zhang and Y. Cui, *Sci. Adv.*, 2016, **2**, e1501764.
61 Y. Kuang, Q. Jia, H. Nishiyama, T. Yamada, A. Kudo and K. Domen, *Adv. Energy Mater.*, 2016, **6**, 1501645.
62 T. W. Kim and K.-S. Choi, *Science*, 2014, **343**, 990–994.
63 W. J. Jo, J. Jang, K. Kong, H. J. Kang, J. Y. Kim, H. Jun, K. P. S. Parmar and J. S. Lee, *Angew. Chem.*, 2012, **124**, 3201–3205.
64 M. Tayebi and B.-K. Lee, *Catal. Today*, 2021, **361**, 183–190.
65 W. Luo, J. Wang, X. Zhao, Z. Zhao, Z. Li and Z. Zou, *Phys. Chem. Chem. Phys.*, 2013, **15**, 1006–1013.
66 C. Zhou, S. Wang, Z. Zhao, Z. Shi, S. Yan and Z. Zou, *Adv. Funct. Mater.*, 2018, **28**, 1801214.
67 H. S. Han, S. Shin, D. H. Kim, I. J. Park, J. S. Kim, P.-S. Huang, J.-K. Lee, I. S. Cho and X. Zheng, *Energy Environ. Sci.*, 2018, **11**, 1299–1306.
68 P. M. Rao, L. Cai, C. Liu, I. S. Cho, C. H. Lee, J. M. Weisse, P. Yang and X. Zheng, *Nano Lett.*, 2014, **14**, 1099–1105.
69 X. Chang, T. Wang, P. Zhang, J. Zhang, A. Li and J. Gong, *J. Am. Chem. Soc.*, 2015, **137**, 8356–8359.
70 Y. Liu, B. R. Wygant, K. Kawashima, O. Mabayoje, T. E. Hong, S. G. Lee, J. Lin, J.-H. Kim, K. Yubuta, W. Li, J. Li and C. B. Mullins, *Appl. Catal., B*, 2019, **245**, 227–239.
71 S. Wang, T. He, J. Yun, Y. Hu, M. Xiao, A. Du and L. Wang, *Adv. Funct. Mater.*, 2018, **28**, 1802685.
72 H. Saada, R. Abdallah, B. Fabre, D. Floner, S. Fryars, A. Vacher, V. Dorcet, C. Meriadec, S. Ababou-Girard and G. Loget, *ChemElectroChem*, 2019, **6**, 613–617.
73 H. She, P. Yue, X. Ma, J. Huang, L. Wang and Q. Wang, *Appl. Catal., B*, 2020, **263**, 118280.
74 D. K. Zhong, S. Choi and D. R. Gamelin, *J. Am. Chem. Soc.*, 2011, **133**, 18370–18377.
75 X. Zhang, R. Wang, F. Li, Z. An, M. Pu and X. Xiang, *Ind. Eng. Chem. Res.*, 2017, **56**, 10711–10719.
76 B. Zhang, X. Huang, Y. Zhang, G. Lu, L. Chou and Y. Bi, *Angew. Chem., Int. Ed.*, 2020, **59**, 18990–18995.
77 W. Zhang, Y. Zhang, H. Yuan, J. Li, L. Ding, S. Chu, L. Wang, W. Zhai and Z. Jiao, *J. Colloid Interface Sci.*, 2022, **616**, 631–640.
78 S. Wang, T. He, P. Chen, A. Du, K. (Ken) Ostrikov, W. Huang and L. Wang, *Adv. Mater.*, 2020, **32**, 2001385.
79 L. Cai, J. Zhao, H. Li, J. Park, I. S. Cho, H. S. Han and X. Zheng, *ACS Energy Lett.*, 2016, **1**, 624–632.
80 Z. Zhang, X. Huang, B. Zhang and Y. Bi, *Energy Environ. Sci.*, 2022, **15**, 2867–2873.
81 Y. Xu, X. Wang, H. Chen, D. Kuang and C. Su, *Adv. Funct. Mater.*, 2016, **26**, 4414–4421.
82 R. Chen, L. Meng, W. Xu and L. Li, *Small*, 2024, **20**, 2304807.
83 D. Tang, J. Liu, X. Wu, R. Liu, X. Han, Y. Han, H. Huang, Y. Liu and Z. Kang, *ACS Appl. Mater. Interfaces*, 2014, **6**, 7918–7925.
84 Z. Gu, J. J. Atherton and Z. P. Xu, *Chem. Commun.*, 2015, **51**, 3024–3036.
85 Z. Li, M. Shao, H. An, Z. Wang, S. Xu, M. Wei, D. G. Evans and X. Duan, *Chem. Sci.*, 2015, **6**, 6624–6631.
86 Y. Wang, D. Yan, S. El Hankari, Y. Zou and S. Wang, *Adv. Sci.*, 2018, **5**, 1800064.

87 D. P. Sahoo, K. K. Das, S. Mansingh, S. Sultana and K. Parida, *Coord. Chem. Rev.*, 2022, **469**, 214666.
88 L. Qian, Z. Lu, T. Xu, X. Wu, Y. Tian, Y. Li, Z. Huo, X. Sun and X. Duan, *Adv. Energy Mater.*, 2015, **469**, 1500245.
89 L. Lv, Z. Yang, K. Chen, C. Wang and Y. Xiong, *Adv. Energy Mater.*, 2019, **9**, 1803358.
90 P. Prabha Sarangi, D. Prava Sahoo, U. Aparajita Mohanty, S. Nayak and K. Parida, *ChemCatChem*, 2024, **16**, e202301533.
91 S. Wang, D. Cui, W. Hao and Y. Du, *Energy Fuel*, 2022, **36**, 11394–11403.
92 Y. Yang, S. Niu, D. Han, T. Liu, G. Wang and Y. Li, *Adv. Energy Mater.*, 2017, **7**, 1700555.
93 J. G. Mavroides, D. I. Tchernev, J. A. Kafalas and D. F. Kolesar, *Mater. Res. Bull.*, 1975, **10**, 1023–1030.
94 C. Jiang, S. J. A. Moniz, A. Wang, T. Zhang and J. Tang, *Chem. Soc. Rev.*, 2017, **46**, 4645–4660.
95 K. Sivula, *J. Phys. Chem. Lett.*, 2013, **4**, 1624–1633.
96 X. Li, J. Yu, J. Low, Y. Fang, J. Xiao and X. Chen, *J. Mater. Chem. A*, 2015, **3**, 2485–2534.
97 M. Kumar, B. Meena, P. Subramanyam, D. Suryakala and C. Subrahmanyam, *NPG Asia Mater.*, 2022, **14**, 88.
98 Y. Li and J. Z. Zhang, *Laser Photonics Rev.*, 2010, **4**, 517–528.
99 Y. Lin, G. Yuan, R. Liu, S. Zhou, S. W. Sheehan and D. Wang, *Chem. Phys. Lett.*, 2011, **507**, 209–215.
100 M. Zhou, X. W. (David) Lou and Y. Xie, *Nano Today*, 2013, **8**, 598–618.
101 Z. Zhang and J. T. Yates, *Chem. Rev.*, 2012, **112**, 5520–5551.
102 C. Ding, J. Shi, Z. Wang and C. Li, *ACS Catal.*, 2017, **7**, 675–688.
103 M. G. Walter, E. L. Warren, J. R. McKone, S. W. Boettcher, Q. Mi, E. A. Santori and N. S. Lewis, *Chem. Rev.*, 2010, **110**, 6446–6473.
104 H. M. Chen, C. K. Chen, R.-S. Liu, L. Zhang, J. Zhang and D. P. Wilkinson, *Chem. Soc. Rev.*, 2012, **4**, 5654.
105 C. Ros, T. Andreu and J. R. Morante, *J. Mater. Chem. A*, 2020, **8**, 10625–10669.
106 X. Liu, J. Chi, B. Dong and Y. Sun, *ChemElectroChem*, 2019, **6**, 2157–2166.
107 R. Abe, *J. Photochem. Photobiol., C*, 2010, **11**, 179–209.
108 A. Kudo and Y. Miseki, *Chem. Soc. Rev.*, 2009, **38**, 253–278.
109 P. Ma and D. Wang, *Nanometerials for Energy Conversion and Storage*, ed. W. Dunwei, and C. Guozhong, World Scientific, Europe, 2018, pp. 1–61.
110 Y. Hou, X. Zhuang and X. Feng, *Small Methods*, 2017, **1**, 1700090.
111 M. R. Nellist, F. A. L. Laskowski, F. Lin, T. J. Mills and S. W. Boettcher, *Acc. Chem. Res.*, 2016, **49**, 733–740.
112 J. Yang, D. Wang, H. Han and C. Li, *Acc. Chem. Res.*, 2013, **46**, 1900–1909.
113 Q. Wang and D. O. Hare, *Chem. Rev.*, 2012, **112**, 4124–4155.
114 F. Cavani, F. Trifirò and A. Vaccari, *Catal. Today*, 1991, **11**, 173–301.
115 G. R. Williams and D. O. Hare, *J. Mater. Chem.*, 2006, **16**, 3065–3074.
116 L. Mohapatra and K. Parida, *J. Mater. Chem. A*, 2016, **4**, 10744–10766.
117 M. Shao, R. Zhang, Z. Li, M. Wei, D. G. Evans and X. Duan, *Chem. Commun.*, 2015, **51**, 15880–15893.
118 X. Zou, A. Goswami and T. Asefa, *J. Am. Chem. Soc.*, 2013, **135**, 17242–17245.
119 M. Gong, Y. Li, H. Wang, Y. Liang, J. Z. Wu, J. Zhou, J. Wang, T. Regier, F. Wei and H. Dai, *J. Am. Chem. Soc.*, 2013, **135**, 8452–8455.
120 F. Song and X. Hu, *J. Am. Chem. Soc.*, 2014, **136**, 16481–16484.
121 (*a*) M. Shao, F. Ning, M. Wei, D. G. Evans and X. Duan, *Adv. Funct. Mater.*, 2014, **24**, 580–586; (*b*) R. A. Krivina, Y. Ou, Q. Xu, L. P. Twight, T. N. Stovall and S. W. Boettcher, *Acc. Mater. Res.*, 2021, **2**, 548–558; (*c*) M. B. Stevens, C. D. M. Trang, L. J. Enman, J. Deng and S. W. Boettcher, *J. Am. Chem. Soc.*, 2017, **139**, 11361–11364; (*d*) L. Trotochaud, S. L. Young, J. K. Ranney and S. W. Boettcher, *J. Am. Chem. Soc.*, 2014, **136**, 6744–6753.
122 M. Laipan, J. Yu, R. Zhu, J. Zhu, A. T. Smith, H. He, D. O'Hare and L. Sun, *Mater. Horiz.*, 2019, **7**, 715–745.
123 R. Gao, J. Zhu and D. Yan, *Nanoscale*, 2021, **13**, 13593–13603.
124 C. G. Silva, Y. Bouizi, V. Fornés and H. García, *J. Am. Chem. Soc.*, 2009, **131**, 13833–13839.
125 S.-M. Xu, T. Pan, Y.-B. Dou, H. Yan, S.-T. Zhang, F.-Y. Ning, W.-Y. Shi and M. Wei, *J. Phys. Chem. C*, 2015, **119**, 18823–18834.
126 Y. Zhu, J. Ren, X. Yang, G. Chang, Y. Bu, G. Wei, W. Han and D. Yang, *J. Mater. Chem. A*, 2017, **5**, 9952–9959.
127 B. J. Trześniewski, O. Diaz-Morales, D. A. Vermaas, A. Longo, W. Bras, M. T. M. Koper and W. A. Smith, *J. Am. Chem. Soc.*, 2015, **137**, 15112–15121.
128 W. He, R. Wang, L. Zhang, J. Zhu, X. Xiang and F. Li, *J. Mater. Chem. A*, 2015, **3**, 17977–17982.
129 R. Li, F. Zhang, D. Wang, J. Yang, M. Li, J. Zhu, X. Zhou, H. Han and C. Li, *Nat. Commun.*, 2013, **4**, 1432.
130 Y. Xu, A. Li, T. Yao, C. Ma, X. Zhang, J. H. Shah and H. Han, *ChemSusChem*, 2017, **10**, 4277–4305.
131 J. Guo, X. Yang, S. Bai, X. Xiang, R. Luo, J. He and A. Chen, *J. Colloid Interface Sci.*, 2019, **540**, 9–19.
132 Y. Zhong, C. Wu, X. Jia, S. Sun, D. Chen, W. Yao, H. Ding, J. Zhang and T. Ma, *J. Chem. Eng.*, 2023, **465**, 142893.
133 Y. Huang, Y. Yu, Y. Xin, N. Meng, Y. Yu and B. Zhang, *Sci. China Mater.*, 2017, **60**, 193–207.
134 (*a*) Z. Zhang and J. T. Yates, *Chem. Rev.*, 2012, **112**, 5520–5551; (*b*) H. L. Tan, R. Amal and Y. H. Ng, *J. Mater. Chem. A*, 2017, **5**, 16498–16521; (*c*) F. A. L. Laskowski, M. R. Nellist, J. Qiu and S. W. Boettcher, *J. Am. Chem. Soc.*, 2019, **141**, 1394–1405.
135 Q. Meng, B. Zhang, H. Yang, C. Liu, Y. Li, A. Kravchenko, X. Sheng, L. Fan, F. Li and L. Sun, *Mater. Adv.*, 2021, **2**, 4323–4332.
136 (*a*) P. Mane, V. Burungale, H. Bae, C. Seong, J. Heo, S. H. Kang and J.-S. Ha, *J. Power Sources*, 2024, **591**, 233832; (*b*) F. Lin and S. W. Boettcher, *Nat. Mater.*, 2014, **13**, 81–86; (*c*) M. Chhetri, S. Dey and C. N. R. Rao, *ACS Energy Lett.*, 2017, **2**, 1062–1069.
137 L. Shi, S. Zhuo, M. Abulikemu, G. Mettela, T. Palaniselvam, S. Rasul, B. Tang, B. Yan, N. B. Saleh and P. Wang, *RSC Adv.*, 2018, **8**, 29179–29188.

138 N. M. Shaddad, M. Hezam, P. Arunachalam, N. M. AL-Saeedan, S. Gimenez, J. Bisquert and A. M. Al-Mayouf, *Mater. Lett.*, 2022, **325**, 132799.
139 X. Chang, T. Wang, P. Zhang, J. Zhang, A. Li and J. Gong, *J. Am. Chem. Soc.*, 2015, **137**, 8356–8359.
140 F. Zhao, N. Li, Y. Wu, X. Wen, Q. Zhao, G. Liu and J. Li, *Int. J. Hydrogen Energy*, 2020, **45**, 31902–31912.
141 T.-G. Vo, Y. Tai and C.-Y. Chiang, *J. Catal.*, 2019, **370**, 1–10.
142 R. Lei, Y. Tang, W. Qiu, S. Yan, X. Tian, Q. Wang, Q. Chen, Z. Wang, W. Qian, Q. Xu, S. Yang and X. Wang, *Nano Lett.*, 2023, **23**, 11785–11792.
143 D. K. Lee and K.-S. Choi, *Nat. Energy*, 2017, **3**, 53–60.
144 R. Gao and L. Wang, *Angew. Chem., Int. Ed.*, 2020, **59**, 23094–23099.
145 R.-T. Gao, N. T. Nguyen, T. Nakajima, J. He, X. Liu, X. Zhang, L. Wang and L. Wu, *Sci. Adv.*, 2023, **9**, eade4589.
146 (*a*) Y. Kuang, Q. Jia, G. Ma, T. Hisatomi, T. Minegishi, H. Nishiyama, M. Nakabayashi, N. Shibata, T. Yamada, A. Kudo and K. Domen, *Nat. Energy*, 2016, **2**, 16191; (*b*) R. Gao, D. He, L. Wu, K. Hu, X. Liu, Y. Su and L. Wang, *Angew. Chem., Int. Ed.*, 2020, **59**, 6213–6218; (*c*) N. An, H. Tian, Y. Zhou, Y. Zou, H. Xiu, Y. Cao, Y. Wang, J. Li, D. Liu and Y. Kuang, *J. Energy Chem.*, 2022, **66**, 657–665; (*d*) S. Jiang, M. Zhang, C. Xu, G. Liu, K. Zhang, Z. Zhang, H.-Q. Peng, B. Liu and W. Zhang, *ACS Nano*, 2024, **18**, 16413–16449; (*e*) T. Wang, Y. Zhang, Y. Zang, Y. Yu, M. Zhuang, W. Zhang and X. Tao, *Ind. Eng. Chem. Res.*, 2023, **62**, 12538–12548.
147 D. He, R.-T. Gao, S. Liu, M. Sun, X. Liu, K. Hu, Y. Su and L. Wang, *ACS Catal.*, 2020, **10**, 10570–10576.
148 L. Wang and F. Xiao, *ChemCatChem*, 2014, **6**, 3048–3052.
149 R. Xu, D. Zhu, K. Du, D. Cui, H. Feng, W. Hao, D. Tian and Y. Du, *Mater. Today Energy*, 2022, **25**, 100961.
150 M. Yu, Z. Wang, J. Liu, F. Sun, P. Yang and J. Qiu, *Nano Energy*, 2019, **63**, 103880.
151 P. Yue, H. She, L. Zhang, B. Niu, R. Lian, J. Huang, L. Wang and Q. Wang, *Appl. Catal., B*, 2021, **286**, 119875.
152 Q. Wang, T. Niu, L. Wang, J. Huang and H. She, *Chin. J. Catal.*, 2018, **39**, 613–618.
153 M. Wang, L. Wu, L. Geng, L. Gao, J. Ge, H. Niu, H. Li and J. Jin, *J. Alloys Compd.*, 2024, **987**, 174183.
154 T. Zhang, Y. Lu, J. Wang, Z. Wang, W. Zhang, X. Wang, J. Su and L. Guo, *Nanotechnology*, 2020, **31**, 115707.
155 P. Wei, Y. Wen, K. Lin and X. Li, *Inorg. Chem. Front.*, 2022, **9**, 4685–4694.
156 M. Chen, X. Chang, Z. Ma, X. Gao and L. Jia, *ACS Appl. Nano Mater.*, 2024, **7**, 15255–15266.
157 D. A. Reddy, K. A. J. Reddy, M. Gopannagari, Y. Kim, A. P. Rangappa, D. P. Kumar and T. K. Kim, *Appl. Surf. Sci.*, 2021, **570**, 151134.
158 T.-G. Vo, K.-F. Chang and C.-Y. Chiang, *J. Catal.*, 2020, **391**, 336–345.
159 X. Wen, M. Fan, Q. Zhao, J. Li and G. Liu, *Chem. – Asian J.*, 2021, **16**, 4095–4102.
160 Z. Huang, X. Cheng, L. Xia, W. Yao, Y. Min, Q. Xu and Q. Wu, *ACS Appl. Nano Mater.*, 2024, **7**, 11655–11665.
161 D. Kim and S.-H. Baek, *Ceram. Int.*, 2024, **50**, 32706–32716.
162 S. Bai, H. Chu, X. Xiang, R. Luo, J. He and A. Chen, *Chem. Eng. J.*, 2018, **350**, 148–156.
163 M. Kolaei, B.-K. Lee and Z. Masoumi, *J. Alloys Compd.*, 2023, **968**, 172133.
164 W. Zhou, T. Jiang, Y. Zhao, C. Xu, C. Pei and H. Xue, *J. Colloid Interface Sci.*, 2019, **549**, 42–49.
165 A. Singh, S. Karmakar and S. Basu, *Int. J. Hydrogen Energy*, 2021, **46**, 39868–39881.
166 S. Bai, J. Han, K. Zhang, J. Sun, J. Guo, R. Luo, D. Li and A. Chen, *ACS Sustainable Chem. Eng.*, 2020, **8**, 4076–4084.
167 J. Jiang, M. Wang, R. Li, L. Ma and L. Guo, *Int. J. Hydrogen Energy*, 2013, **38**, 13069–13076.
168 G. Dong, T. Chen, F. Kou, F. Xie, C. Xiao, J. Liang, C. Lou, J. Zhuang and S. Du, *Nanomaterials*, 2024, **14**, 1100.
169 B. Kang, M. Bilal Hussain, X. Cheng, C. Peng and Z. Wang, *J. Colloid Interface Sci.*, 2022, **626**, 146–155.
170 H. Li, M. Lyu, X. Cheng, Y. Lai and Z. Dong, *J. Catal.*, 2023, **428**, 115203.
171 G. Yin, C. Liu, T. Shi, D. Ji, Y. Yao and Z. Chen, *J. Photochem. Photobiol., A*, 2022, **426**, 113742.
172 J. Zhang, L. Wang, M. Li, Z. Zhang, M. Yang, H. Wu, Q. Zhang and X. Xu, *J. Alloys Compd.*, 2023, **965**, 171508.
173 T. Wang, H. Pei, Y. Zhang, R. Li, J. Zhang and T. Peng, *ACS Appl. Energy Mater.*, 2022, **5**, 11271–11282.
174 C. Liu, Y. Zhang, G. Yin, T. Shi, Y. Zhang and Z. Chen, *Inorg. Chem. Front.*, 2022, **9**, 6431–6440.
175 M. K. Mohanta, T. K. Sahu, S. Bhowmick and M. Qureshi, *Electrochim. Acta*, 2022, **415**, 140269.
176 H. Pei, S. Xu, Y. Zhang, Y. Zhou, R. Li and T. Peng, *Appl. Catal., B*, 2022, **318**, 121865.
177 X. Han, Y. Wei, J. Su and Y. Zhao, *ACS Sustainable Chem. Eng.*, 2018, **6**, 14695–14703.
178 L. Sun, J. Sun, X. Yang, S. Bai, Y. Feng, R. Luo, D. Li and A. Chen, *Dalton Trans.*, 2019, **48**, 16091–16098.
179 S. Alam and M. Qureshi, *J. Phys. Chem. Lett.*, 2021, **12**, 8947–8955.
180 H. Chen, S. Wang, J. Wu, X. Zhang, J. Zhang, M. Lyu, B. Luo, G. Qian and L. Wang, *J. Mater. Chem. A*, 2020, **8**, 13231–13240.
181 R. Wang, L. Luo, X. Zhu, Y. Yan, B. Zhang, X. Xiang and J. He, *ACS Appl. Energy Mater.*, 2018, **1**, 3577–3586.
182 W. Bai, H. Li, Y. Hu, J. Wang, A. Li and P. François-Xavier Corvini, *Chem. Eng. J.*, 2024, **479**, 147713.
183 W. Chen, G. Jin, Y. Liu, Q. Wei and J. Tang, *ACS Appl. Mater. Interfaces*, 2024, **16**, 23296–23304.
184 X. Lv, X. Xiao, M. Cao, Y. Bu, C. Wang and M. Wang, *Appl. Surf. Sci.*, 2018, **439**, 1065–1071.
185 Y. Tang, R. Wang, Y. Yang, D. Yan and X. Xiang, *ACS Appl. Mater. Interfaces*, 2016, **8**, 19446–19455.
186 Y. Sun, H. Li, Y. Hu, J. Wang, A. Li and P. F.-X. Corvini, *Appl. Catal., B*, 2024, **340**, 123269.
187 M. Gao, N. T. Nguyen, R.-T. Gao, X. Liu, X. Zhang and L. Wang, *Appl. Catal., B*, 2023, **336**, 122920.
188 S. Feng, S. Fan, L. Li, Z. Sun, H. Tang, Y. Xu, L. Fang and C. Wang, *Nano Res. Energy*, 2024, **3**, e9120117.

189 M. Xu and M. Wei, *Adv. Funct. Mater.*, 2018, **28**, 1802943.
190 D. Friebel, M. W. Louie, M. Bajdich, K. E. Sanwald, Y. Cai, A. M. Wise, M.-J. Cheng, D. Sokaras, T.-C. Weng, R. Alonso-Mori, R. C. Davis, J. R. Bargar, J. K. Nørskov, A. Nilsson and A. T. Bell, *J. Am. Chem. Soc.*, 2015, **137**, 1305–1313.
191 L. Chen, H. Zhang, L. Chen, X. Wei, J. Shi and M. He, *J. Mater. Chem. A*, 2017, **5**, 22568–22575.
192 L. Yu, J. F. Yang, B. Y. Guan, Y. Lu and X. W. (David) Lou, *Angew. Chem.*, 2018, **130**, 178–182.
193 C. Zhang, M. Shao, L. Zhou, Z. Li, K. Xiao and M. Wei, *ACS Appl. Mater. Interfaces*, 2016, **8**, 33697–33703.
194 G. Jia, Y. Hu, Q. Qian, Y. Yao, S. Zhang, Z. Li and Z. Zou, *ACS Appl. Mater. Interfaces*, 2016, **8**, 14527–14534.
195 M. Guo, L. Zhou, Y. Li, Q. Zheng, F. Xie and D. Lin, *J. Mater. Chem. A*, 2019, **7**, 13130–13141.
196 H. Liu, Y. Wang, X. Lu, Y. Hu, G. Zhu, R. Chen, L. Ma, H. Zhu, Z. Tie, J. Liu and Z. Jin, *Nano Energy*, 2017, **35**, 350–357.
197 J. Bao, Z. Wang, J. Xie, L. Xu, F. Lei, M. Guan, Y. Zhao, Y. Huang and H. Li, *Chem. Commun.*, 2019, **55**, 3521–3524.
198 R. A. Sayed, S. E. Abd El Hafiz, N. Gamal, Y. GadelHak and W. M. A. el Rouby, *J. Alloys Compd.*, 2017, **728**, 1171–1179.
199 R. Chong, B. Wang, C. Su, D. Li, L. Mao, Z. Chang and L. Zhang, *J. Mater. Chem. A*, 2017, **5**, 8583–8590.
200 R. Zhang, M. Shao, S. Xu, F. Ning, L. Zhou and M. Wei, *Nano Energy*, 2017, **33**, 21–28.
201 G. Wang, B. Wang, C. Su, D. Li, L. Zhang, R. Chong and Z. Chang, *J. Catal.*, 2018, **359**, 287–295.
202 K. Fan, H. Chen, Y. Ji, H. Huang, P. M. Claesson, Q. Daniel, B. Philippe, H. Rensmo, F. Li, Y. Luo and L. Sun, *Nat. Commun.*, 2016, **7**, 11981.
203 X. Long, S. Xiao, Z. Wang, X. Zheng and S. Yang, *Chem. Commun.*, 2015, **51**, 1120–1123.
204 X. Yang, J. Cui, L. Lin, A. Bian, J. Dai, W. Du, S. Guo, J. Hu and X. Xu, *Adv. Sci.*, 2024, **11**, 2305567.
205 H. Zhang, H. Li, Z. Wang, Z. Zheng, P. Wang, Y. Liu, X. Zhang, X. Qin, Y. Dai and B. Huang, *Appl. Catal., B*, 2018, **238**, 586–591.
206 T. Soltani, A. Tayyebi and B.-K. Lee, *Sol. Energy Mater. Sol. Cells*, 2018, **185**, 325–332.
207 J. Li, J. Bai, X. Niu, X. Li, S. Chen, J. Wang and B. Zhou, *Int. J. Hydrogen Energy*, 2018, **43**, 18202–18210.
208 D. Chen, Z. Liu, Z. Guo, W. Yan and Y. Xin, *J. Mater. Chem. A*, 2018, **6**, 20393–20401.
209 X. Wu, J. Zhao, S. Guo, L. Wang, W. Shi, H. Huang, Y. Liu and Z. Kang, *Nanoscale*, 2016, **8**, 17314–17321.
210 P. Hemmatpour and A. Nezamzadeh-Ejhieh, *Chemosphere*, 2022, **307**, 135925.
211 S. J. A. Moniz, S. A. Shevlin, D. J. Martin, Z.-X. Guo and J. Tang, *Energy Environ. Sci.*, 2015, **8**, 731–759.
212 S. Bai, Q. Li, J. Han, X. Yang, X. Shu, J. Sun, L. Sun, R. Luo, D. Li and A. Chen, *Int. J. Hydrogen Energy*, 2019, **44**, 24642–24652.
213 K. Sivula, F. Le Formal and M. Grätzel, *ChemSusChem*, 2011, **4**, 432–449.
214 S. Wang, B. Liu, X. Wang, Y. Zhang and W. Huang, *Nano Res.*, 2022, **15**, 7026–7033.
215 M. B. Costa, M. A. de Araújo, M. V. de Tinoco, J. F. de Brito and L. H. Mascaro, *J. Energy Chem.*, 2022, **73**, 88–113.
216 D. Sharma, S. Upadhyay, A. Verma, V. R. Satsangi, R. Shrivastav and S. Dass, *Thin Solid Films*, 2015, **574**, 125–131.
217 L. Banszerus, M. Schmitz, S. Engels, J. Dauber, M. Oellers, F. Haupt, K. Watanabe, T. Taniguchi, B. Beschoten and C. Stampfer, *Sci. Adv.*, 2015, **1**, e1500222.
218 S. Linic, P. Christopher and D. B. Ingram, *Nat. Mater.*, 2011, **10**, 911–921.
219 H. M. Chen, C. K. Chen, C.-J. Chen, L.-C. Cheng, P. C. Wu, B. H. Cheng, Y. Z. Ho, M. L. Tseng, Y.-Y. Hsu, T.-S. Chan, J.-F. Lee, R.-S. Liu and D. P. Tsai, *ACS Nano*, 2012, **6**, 7362–7372.
220 S.-J. Lin, K.-C. Lee, J.-L. Wu and J.-Y. Wu, *Sol. Energy*, 2012, **86**, 2600–2605.
221 Y. Sun, S. Gao and Y. Xie, *Chem. Soc. Rev.*, 2014, **4**, 530–546.
222 B. J. Trześniewski, I. A. Digdaya, T. Nagaki, S. Ravishankar, I. Herraiz-Cardona, D. A. Vermaas, A. Longo, S. Gimenez and W. A. Smith, *Energy Environ. Sci.*, 2017, **10**, 1517–1529.
223 J. Pina, P. Dias, C. Serpa, J. Azevedo, A. Mendes and J. Sérgio Seixas de Melo, *J. Phys. Chem. C*, 2021, **125**, 8274–8284.
224 X. Liu, G. Dong, S. Li, G. Lu and Y. Bi, *J. Am. Chem. Soc.*, 2016, **138**, 2917–2920.
225 J. Hu, X. Zhao, W. Chen, H. Su and Z. Chen, *J. Phys. Chem. C*, 2017, **121**, 18702–18709.
226 M. Huang, S. Wang and H. Zhu, *J. Mater. Chem. A*, 2023, **11**, 21619–21627.
227 Z. Wang, Y. Gu, L. Zheng, J. Hou, H. Zheng, S. Sun and L. Wang, *Adv. Mater.*, 2022, **34**, 2106776.
228 Y. Pihosh, I. Turkevych, K. Mawatari, J. Uemura, Y. Kazoe, S. Kosar, K. Makita, T. Sugaya, T. Matsui, D. Fujita, M. Tosa, M. Kondo and T. Kitamori, *Sci. Rep.*, 2015, **5**, 11141.
229 J. H. Kim, Y. Jo, J. H. Kim, J. W. Jang, H. J. Kang, Y. H. Lee, D. S. Kim, Y. Jun and J. S. Lee, *ACS Nano*, 2015, **9**, 11820–11829.
230 Y. Zhang, H. Lv, Z. Zhang, L. Wang, X. Wu and H. Xu, *Adv. Mater.*, 2021, **33**, 2008264.
231 S. Ye, W. Shi, Y. Liu, D. Li, H. Yin, H. Chi, Y. Luo, N. Ta, F. Fan, X. Wang and C. Li, *J. Am. Chem. Soc.*, 2021, **143**, 12499–12508.

